Entrained flow gasification: pilot-scale experimental, balancing and equilibrium data for model validation

Maximilian Dammann[a,b,c,*], Ulrike Santo[b], David Böning[b], Hannah Knoch[b],
Mark Eberhard[b], Thomas Kolb[a,b]

[a]*Karlsruhe Institute of Technology (KIT), Engler-Bunte-Institute, Fuel Technology
(EBI ceb), Engler-Bunte-Ring 1, 76131 Karlsruhe, Germany*
[b]*Karlsruhe Institute of Technology (KIT), Institute for Technical Chemistry, Gasification
Technology (ITC vgt), Hermann-von-Helmholtz-Platz 1, 76344 Eggenstein-Leopoldshafen,
Germany*
[c]*Clausthal University of Technology, Institute for Energy Process Engineering and Fuel
Technology (IEVB), Agricolastrasse 4, 38678 Clausthal-Zellerfeld, Germany*

Abstract

Biogenic and anthropogenic feedstocks can be converted into high-quality and hydrogen-rich synthesis gas through high-pressure entrained flow gasification. However, robust pilot-scale process data is essential for the optimisation, design and scale-up of this process. Therefore, this study conducted pilot-scale experiments, developed balancing and equilibrium models for performance analysis and derived input and validation data for CFD models. The experiments were carried out at the bioliq Entrained Flow Gasifier plant using mixtures of ethylene glycol or beech wood pyrolysis oil with glass beads, thermal inputs of up to 5 MW and operating pressures of 40 bar. The cooling screen was recoated before the experiments to ensure well-defined heat transfer conditions. The data from on-line measurements and off-line analyses was evaluated with emphasis on the synthesis gas condition before quenching, the heat extraction from the inner reactor chamber and the carbon conversion. The results show that the balancing model provides consistent and accurate predictions and the equilibrium model is able to track the generated process data. Specifically, the balancing predictions are accurate if the solution of CO_2

*Corresponding author.
ORCID: https://orcid.org/0000-0002-2851-7787.

in the quench water is accounted for, if undetected intermediates are described as lost carbon and lost atomic hydrogen and if further chemical reactions in the quench water are avoided by appropriate operating conditions.

Nomenclature

Latin symbols

A	area
c	mass concentration
$\hat{H}$	specific enthalpy
K	constant
$\dot{m}$	mass flow rate
$\dot{n}$	molar flow rate
p	pressure
P	input
$\dot{q}$	heat flux
$\dot{\boldsymbol{q}}$	heat flux vector
$\dot{Q}$	heat flow rate
$\dot{\boldsymbol{Q}}$	heat flow rate vector
T	temperature
w	mass fraction
$\boldsymbol{w}$	mass fraction vector
x	mole fraction
$\boldsymbol{x}$	mole fraction vector

Greek symbols

Δ	difference, uncertainty
κ	electrical conductivity
λ	stoichiometric ratio
ρ	density

Subscripts and superscripts

A	at position A
aq	aqueous
ash	of ash
asr	on as-received basis
at	based on the ash tracer method
B	at position B
bal	balanced
Boie	based on the Boie correlation
C	at position C
calc	calculated
csp	in the purge stream for the cooling screen
diss	dissociation
dry	on dry basis
eq	equilibrium, equilibrium-derived
fuel	of fuel, in fuel
gas	gas, in the gas
i	of species i
in	at inlet
loss	lost
meas	measured

ng	of natural gas
ngb	at natural gas burner
op	operating
out	at outlet
quench	in the quench water
s	surface
sb	at slurry burner
Si	of segment i
slag	of slag, in slag
slurry	of slurry
steam	of steam
th	thermal
TOC	of total organic carbon
top	top
wall	wall
water	of liquid water
WGS	water-gas shift
ww	based on the waste water method
ww+ash	based on both the waste water method and the ash tracer method
ww,quench	of the waste water stream of the quench
ww,scrubber	of the waste water stream of the Venturi scrubber

Acronyms

bioliq EFG	bioliq Entrained Flow Gasifier
CC	carbon conversion
CFD	computational fluid dynamics

4

CGE	cold gas efficiency
CO2L	loss of dissolved and dissociated CO_2 with the discharged waste water
FZK	Forschungszentrum Karlsruhe
GC	gas chromatography
HCR	atomic hydrogen/carbon ratio
HHV	higher heating value
IAPWS	International Association for the Properties of Water and Steam
KIT	Karlsruhe Institute of Technology
LHV	lower heating value
MHI EFG	Mitsubishi Heavy Industries Entrained Flow Gasifier
PEHT-BLG	Pressurised Entrained flow High-Temperature Black Liquor Gasifier
SMOD	specific minimum oxygen demand
Texaco EFG	Texaco Entrained Flow Gasifier
TIC	total inorganic carbon
TOC	total organic carbon
TUBAF HP-POX	Technical University Bergakademie Freiberg High-Pressure Partial OXidation gasifier
WGS	water-gas shift
Y	synthesis gas yield

1. Introduction

Entrained flow gasification of biogenic and anthropogenic feedstocks is one of the promising technologies for the production of renewable liquid fuels and chemicals in closed-carbon cycle economies and the reduction of

CO_2 emissions in the long-distance transport sector [1, 2]. In order to optimise and scale-up this technology, the bioliq pilot plant [3] was built up and commissioned at Forschungszentrum Karlsruhe (FZK) / Karlsruhe Institute of Technology (KIT) between 2005 and 2013 in a collaboration between institutes of FZK/KIT, industrial partners and public funding agencies [4]. The bioliq pilot plant represents the bioliq process [1] and consists of four stages: (i) fast pyrolysis and slurry production, (ii) high-pressure gasification, (iii) gas cleaning and gas conditioning and (iv) gas synthesis [4].

The main unit of the high-pressure gasification (see Fig. 1) is the bioliq Entrained Flow Gasifier (bioliq EFG) with a thermal input of up to 5 MW [4]. The bioliq EFG is applied to convert suspension fuels with high mineral contents, such as pyrolysis oil-char slurries, into raw synthesis gas, where oxygen and steam are used as gasification media [4]. Furthermore, nitrogen is fed to the inner reactor chamber (marked with a yellow line in Fig. 1) for purging, and natural gas for ignition and flame stabilisation [4]. The inner reactor chamber of the bioliq EFG is enveloped by a refractory made of SiC and a segmental cooling screen. Six water cooling circuits are applied for the main heat extraction [4]. Two further water cooling circuits are used to ensure proper cooling of the slurry burner and the natural gas burner [4]. The mineral particles deposit together with soot and incompletely converted carbonaceous particles on the refractory and form liquid, crystalline and solidified slag phases [5]. The molten slag flows down the refractory and leaves the inner reactor chamber together with the raw synthesis gas at position B (see Fig. 1) [4]. A dip water quench with annular nozzles is used for the cooling of both the slag and the raw synthesis gas from over 1500 K to less than 500 K, leading in particular to (i) condensation or vaporisation of water and (ii) partial solution and dissociation of the other gas species in the quench water. Measurements of the synthesis gas composition are conducted using mass spectroscopy at position E (see Fig. 1) and using gas chromatography after several separation units at position C (see Fig. 1) [4].

Accurate data of gas temperatures and gas species concentrations from

the inner reactor chamber is essential for performance analysis, optimisation, design and scale-up of entrained flow gasification processes. Therefore, Chen et al. [6] measured gas temperatures at the MHI Entrained Flow Gasifier (MHI EFG), while Marklund [7] and Wiinikka et al. [8] developed methods and probes for measuring gas temperatures and gas species concentrations inside the CHEMREC Pressurised Entrained High Temperature-Black Liquor Gasifier (CHEMREC PEHT-BLG). However, such measurements are elaborative at both pilot-scale and full-scale entrained flow gasifiers with quench configurations due to the high-temperature, high-pressure, corrosive and slagging conditions. Therefore, synthesis gas compositions are typically measured far from the inner reactor chamber using standard methods, while balancing methods are essential (i) to determine the synthesis gas condition and the carbon conversion at the outlet of the inner reactor chamber (at position B in the case of the bioliq EFG, see Fig. 1), (ii) to reflect the changes in the synthesis gas composition between the outlet of the inner reactor chamber and the gas measurement unit (between positions B and C in the case of the bioliq EFG, see Fig. 1) and (iii) to obtain reliable experimental data for validation of methods that can be applied for optimisation, design and scale-up.

Several studies [4, 8, 9, 10, 11, 12, 13, 14, 15, 16, 17] have outlined balancing methods that relied on elemental balances and corrections. Robin [13] adjusted the experimental data within standard uncertainties to close the elemental balances. Richter et al. [14] mentioned corrections for the steam saturation of the synthesis gas stream leaving the quench system. Brueggemann [10] investigated the carbon conversion for the gasification of natural gas, light oil and heavy oil at the Technical University Bergakademie Freiberg High-Pressure Partial OXidation gasifier (TUBAF HP-POX) accounting for several by-products including ammonia, hydrocyanic and formic acid. Roberts et al. [18, 19] derived carbon conversions from measured gas species concentrations for the gasification of coal at both laboratory-scale and pilot-scale plants. Jafri et al. [20, 21], in turn, determined the carbon

7

conversion using the total organic carbon content in the discharged quench water stream. However, these previous studies did not provide many details on balances and corrections or partly neglected changes of the dry synthesis gas composition between the gasification unit and the measurement unit. Furthermore, numerous studies on entrained flow gasification processes with quench configurations [22, 23, 24, 25, 26, 27, 28, 29, 30, 31] applied industrial measurement results for performance analysis and validation neglecting any changes of the dry synthesis gas composition. However, accurate modelling and balancing approaches are crucial as Wiinikka et al. [17] already showed that the synthesis gas composition could significantly change in the quench system of the CHEMREC PEHT-BLG due to both the water-gas shift reaction and the solution of CO_2.

Measurements and balancing methods are usually accompanied by further modelling efforts using equilibrium models, one-dimensional plug-flow models, further reduced order models or CFD models. Equilibrium models (e.g. [32, 33, 34, 35, 36, 37, 38, 39]), one-dimensional plug-flow models (e.g. [32, 40, 41, 42, 43, 44, 45, 46]) and further reduced order models (e.g. [9, 47, 48, 49, 50, 51, 52, 53]) are simplified, fast-computing approaches. Kong et al. [37], for example, developed an equilibrium model for the Texaco EFG with units for pyrolysis and combustion, char gas reaction and gas phase reaction, where the steam stream was split to obtain accurate predictions of the measured carbon conversions. Moreover, Covella et al. [12] coupled data reconciliation with equilibrium calculations to reduce the errors and uncertainties in the balances from several previous bioliq EFG experiments (typically closed with errors less than 3 % [4]). Other studies constrained carbon conversion, methane content or trace element contents [32, 33, 34] or specified temperatures above which full equilibrium is achieved [35, 36, 37, 38, 39] to adjust the equilibrium results. Thus, in the absence of superior approaches, equilibrium and reduced-order models were often coupled with empirical adjustments to reduce the deviations between measured and predicted gas species concentrations. Superior approaches could be CFD models

(e. g. [6, 7, 33, 54, 55, 56, 57, 58]). Such models are used to provide insight into the physical and thermo-chemical sub-processes and can be used for the prediction of the heat extraction from entrained flow gasification processes even if equilibrium conditions can be expected for large parts of the inner reactor chamber. However, the mathematical description of the heat extraction through slag layers and refractory has never been validated due to the lack of appropriate validation data sets. Moreover, it is difficult to identify the best approach for the thermal wall boundary conditions and to improve slag flow models.

Thus, there is significant lack of balancing methods accounting for the impact of the quench on the synthesis gas composition and of validation data sets for entrained flow gasification processes. Furthermore, almost all previous pilot-scale studies focussed on entrained flow gasification processes with fossil fuels, whereas data from pilot-scale experiments with surrogate and technical biogenic fuels is scarce. Therefore, this study (i) conducted pilot-scale experiments using mixtures of ethylene glycol or beech wood pyrolysis oil with glass beads, (ii) developed balancing and equilibrium models and (iii) derived input and validation data for CFD models. The focus of this study is in particular on the verification of the balancing and equilibrium models through the application to four experiments and the analysis of the influences on synthesis gas quality between positions B and C (see Fig. 1). The balancing model is based on both elemental and energy balances and measurements and was developed for performance analysis and retrospective calculation of the gas condition at the outlet of the inner reactor chamber (at position B, see Fig. 1). In contrast, the equilibrium model relies on both elemental and energy balances and equilibrium calculations and was developed for the design and scale-up of experiments and the verification of balancing results. The influences on synthesis gas quality at positions B and C are explained in Section 2. The experiments and the balancing and equilibrium models are described in Section 3, while the results of the experiments and the process calculations are presented alongside sensitivity analyses in Section 4. The conclusions are given

9

in Section 5.

2. Influences on synthesis gas quality

The balancing approach developed in this study is based on the idea that the measured synthesis gas composition at position C can be used to derive the synthesis gas composition at position B (see Fig. 1). However, the synthesis gas composition at position C is affected by the operating parameters of the entrained flow gasifier, the quench and the Venturi scrubber [11, 17] and by numerous processes, including (i) the formation and degradation of intermediates and by-products, (ii) the water-gas shift (WGS) reaction and (iii) the solution and dissociation of synthesis gas species in the quench water.

2.1. Intermediates and by-products

Intermediates are hydrocarbons with different H/C ratios and carbonaceous particles from the decomposition and the conversion of fuel components. Such intermediates can be found in the synthesis gas due to the non-ideal conditions in technical systems such as insufficient residence times or non-ideal atomisation and mixing behaviours. The formation and the degradation of intermediates in gasifiers primarily affect the synthesis gas composition due to consumption or production of major synthesis gas species. With increasing amounts of intermediates, the higher degree of oxidation of the major gas species resulting from the incomplete conversion of intermediates leads to an increase in the synthesis gas temperature. Due to the adjustment of the endothermic WGS equilibrium, the increased synthesis gas temperature additionally shifts the synthesis gas composition and leads to higher gas species concentrations of CO and H_2O (see Section 2.2).

By-products such as NH_3 and HCN are formed in gasifiers from components bound in the fuel and from purge nitrogen under both ideal and non-ideal operating conditions (see Section 4.2.3).

Some of the intermediates and by-products are separated from the synthesis

10

gas in the quench and can be found in the quench water or in the solidified slag residues. In addition, further by-products such as formic acid are formed in the quench from the synthesis gas species enhanced by the presence of basic components such as NH_3 and NaOH [10, 59]. In this study, however, CH_4 and C(s) were accounted for as intermediates in the elemental balancing only (see Section 3.4).

2.2. Water-gas shift reaction

The endothermic WGS reaction is significantly faster than the formation and degradation of hydrocarbons and carbonaceous particles and thus determines the concentrations of the major gas species of the synthesis gas that leaves the inner reactor chamber. The WGS equilibrium is described by [60]

$$CO + H_2O \rightleftharpoons CO_2 + H_2 \tag{1}$$

and can be mathematically determined using the temperature dependent WGS equilibrium constant $K_{eq,WGS}$ from the equilibrium gas species mole fractions of CO, CO_2, H_2 and H_2O. The corresponding inverse relationship $T_{WGS}(K_{eq,WGS})$ provides the WGS temperature T_{WGS} [61] and was established in this study using data from Aspen Properties [62]. The WGS temperature T_{WGS} is identical to the gas temperature at the outlet of the inner reactor chamber (position B) if the partial WGS equilibrium is reached at the outlet and the WGS temperature T_{WGS} is calculated using the gas composition at the outlet. However, the synthesis gas composition changes due to rapid cooling, condensation and vaporisation when the synthesis gas passes the quench and the Venturi scrubber. With cooling, the WGS reaction slows down until the cooling process is faster than the adjustment of the WGS equilibrium. Depending on (i) the cooling rate which is typically determined by the mass flow rate ratio of the water stream in the first spray ring to the synthesis gas stream [17], (ii) the operating pressure [17] and (iii) the amounts of steam and catalytic components in gas, the WGS reaction freezes below a certain freezing temperature, i.e. the dry gas species concentrations

11

of the WGS reactants do not change any more (see Section S3). If the gas temperature at the outlet is below this temperature and gas solution processes in the quench water can be neglected, the dry synthesis gas composition undergoes minimal change when passing the quench. Thus, if the gas species concentrations of CO, CO_2, H_2 and H_2O at the outlet are known and if a partial WGS equilibrium can be assumed at the outlet, the predicted gas temperature T_{gas} at the outlet can be verified with the WGS temperature T_{WGS} at the outlet. However, if the gas temperature T_{gas} at the outlet is above the freezing temperature, the gas temperature T_{gas} at the outlet and the WGS temperature T_{WGS} at the outlet differ as the WGS equilibrium still adjusts outside the inner reactor chamber. Therefore, the freezing temperature should be above the highest WGS temperature determined for entrained flow gasification experiments with well-defined fuels and similar quench operating conditions.

2.3. Solution of synthesis gas species in quench water

The processes occurring in a water quench include (i) the rapid cooling of synthesis gas to temperatures below $500\,K$ through large amounts of water, (ii) the saturation of synthesis gas with water vapour and (iii) the solution and dissociation of synthesis gas species in the quench water [17]. However, the cooling, condensation and vaporisation processes do not affect the dry synthesis gas composition if the gas temperature T_{gas} at the outlet is below the freezing temperature of the WGS reaction (see Section 2.2). Only the solution and dissociation of synthesis gas species in the quench water have an impact on the dry synthesis gas composition and therefore on the elemental balancing (see Section 3.4). As low fractions of dissolved and dissociated synthesis gas species accumulate in the quench water and are discontinuously discharged with the waste waters of the quench and the Venturi scrubber (see Section S4), the synthesis gas composition changes in accordance with the different solubilities of the synthesis gas species in the quench water. In particular, CO_2 and even more NH_3 show higher physical solubilities than the other gas species

12

(see Fig. S4). Furthermore, the acid-base equilibrium between dissolved CO_2 and NH_3 enhances the solution and the dissociation of both species [63], i.e. NH_3 captures CO_2 in the quench water (see Section S5.1). However, in this study, as very low amounts of ammonia are expected to be present in the synthesis gas, the solution of CO_2 is accounted for in the elemental balancing only (see Section 3.4).

3. Methods

This section describes the experiments and the methods developed and optimised since the construction of the bioliq EFG plant to evaluate experimental data and to derive balancing and equilibrium data.

3.1. Experiments

The focus of this study is on the campaign with the bioliq EFG experiments V82[1], V83, V84 and V85. The experiments and the characteristic operating parameters are summarised in Table 1.

Table 1: Characteristic operating parameters: slurry, thermal input of slurry $P_{\text{th,slurry}}$, thermal input of natural gas $P_{\text{th,ng}}$, operating pressure p_{op}, ash/slurry mass flow rate ratio $\dot{m}_{\text{ash}}/\dot{m}_{\text{slurry}}$, steam/slurry mass flow rate ratio $\dot{m}_{\text{steam}}/\dot{m}_{\text{slurry}}$, oxygen/slurry mass flow rate ratio $\dot{m}_{\text{O}_2}/\dot{m}_{\text{slurry}}$, nitrogen/slurry mass flow rate ratio $\dot{m}_{\text{N}_2}/\dot{m}_{\text{slurry}}$ and stoichiometric ratio λ.

Experiment	Slurry	$\dfrac{P_{\text{th,slurry}}}{\text{MW}}$	$\dfrac{P_{\text{th,ng}}}{\text{MW}}$	$\dfrac{p_{\text{op}}}{\text{bar}}$	$\dfrac{\dot{m}_{\text{ash}}}{\dot{m}_{\text{slurry}}}$	$\dfrac{\dot{m}_{\text{steam}}}{\dot{m}_{\text{slurry}}}$	$\dfrac{\dot{m}_{\text{O}_2}}{\dot{m}_{\text{slurry}}}$	$\dfrac{\dot{m}_{\text{N}_2}}{\dot{m}_{\text{slurry}}}$	λ
V82	Ethylene glycol + glass beads	3.5	0.5	40	0.045	0.38	0.79	0.22	0.553
V83	Ethylene glycol + glass beads	3.5	0.5	40	0.045	0.38	0.74	0.24	0.521
V84	Ethylene glycol + glass beads	3.3	0.5	40	0.090	0.38	0.78	0.26	0.571
V85	Beech wood pyrolysis oil + glass beads	4.4	0.5	40	0.046	0.40	0.88	0.29	0.465

---

[1]The (first) stationary operating point of the bioliq EFG experiment V82 was already described as bioliq EFG experiment V82.1 in previous studies [2, 64, 65, 66] and is referred as stationary operating point of the bioliq EFG experiment V82 in this study. However, the reported data differs as revised methods were applied in this study to improve the experimental, balancing and equilibrium data.

The bioliq EFG experiments V82, V83 and V84 were short-term experiments with mixtures of ethylene glycol and glass beads (stationary input for 6 h). Ethylene glycol and glass beads were applied as surrogates for pyrolysis oil and straw ash, respectively [2, 64], enabling reproducible experiments and numerical modelling due to well-defined chemical and physical properties compared to technical materials. Moreover, ethylene glycol has a C/H/O ratio and a heating value similar to typical biomass pyrolysis oils [61], while glass beads have low constant catalytic activities compared to biomass ash and ensure slag deposition and therefore protection of the refractory material of the cooling screen. Furthermore, the bioliq EFG experiment V82 was defined as near-equilibrium reference experiment to ensure high temperatures, high carbon conversions and low methane concentrations in the synthesis gas. In contrast, the bioliq EFG experiment V83 and the bioliq EFG experiment V84 were used to investigate the influence of a lower stoichiometric ratio and the influence of the glass content, respectively. Finally, the bioliq EFG experiment V85 was a long-term experiment with beech wood pyrolysis oil and glass beads (stationary input for 100 h) to provide synthesis gas for downstream fuel synthesis. The beech wood pyrolysis oil is a by-product of the charcoal production and was purchased from proFagus [67], while the glass beads were supplied due to the low ash content of the pyrolysis oil.

The bioliq EFG experiments V82, V83, V84 and V85 were thus based on multiple-variable design as the operational constraints limited the period of time for extensive experimental investigation. However, these experiments could be conducted under well-defined heat transfer conditions and were therefore selected to demonstrate the applicability of both the balancing model and the equilibrium model. Specifically, (i) the refractory of the cooling screen was rebuilt before the campaign (which included the removal of previous slag depositions), (ii) the new slag deposition was realised through glass beads with approximately uniform chemical and physical properties and (iii) the refractory was exposed neither to temperatures close to the temperature resistance limits nor to additives during the campaign. In particular, corrosion of the refractory

material was not observed during visual examination before and after the experiments. Furthermore, the campaign was connected with elaborative slag characterisation experiments drawing on previous studies [5, 68, 69]. These experiments are described in the subsequent study [70]. Specifically, the thickness of the solidified slag deposition was investigated under ambient conditions immediately after the bioliq EFG experiments V82, V83 and V84. Both studies thus provide unique data sets for validation of CFD models.

3.1.1. Continuous measurements

The measurements were continuously performed at 250 measurement points. Specifically, (i) the mass flow rates, temperatures and pressures of both the feed streams and the process water streams, (ii) the refractory temperatures at positions T1, ..., T10 (see Fig. 2) and (iii) the dry gas species concentrations of CH_4, CO, CO_2, H_2 and N_2 in the synthesis gas stream at positions C and E (see Fig. 1) were recorded during the campaign.

The flow rates of the streams were determined using the flow metres listed in Table S4. The temperatures and pressures of the streams were measured using resistance thermometers (Schramm WME) and pressure transducers (Endress+Hauser Cerabar S PMP), respectively, while the refractory temperatures were obtained using shielded type K thermocouples. The dry gas species concentrations in the synthesis gas stream were measured using gas chromatography (Emerson Danalyser 700) at position C and mass spectroscopy (Extrel MAX300-IG) at position E. The gas chromatograph was calibrated using reference gases before reaching stationary conditions (see Sections 3.2 and S6) and provided accurate measurement data in time intervals of 5 minutes, whereas the measurement data based on mass spectroscopy was not used in this study as the data accuracy has not been sufficient.

3.1.2. Analyses

Samples of beech wood pyrolysis oil, slag and waste waters were collected during the bioliq EFG experiments for further analysis. The beech

wood pyrolysis oil samples were characterised at ten internal and external laboratories. The chemical properties were determined using the standards listed in Tables S5-S7. The slag samples were taken at position D and analysed with respect to carbon, sulphur and chlorine contents, whereas further slag analyses are reported for the bioliq EFG experiments V82, V83, V84 and V85 in the subsequent study [70]. The waste water samples were collected at positions F and G. Due to the discontinuous operating modes of both the quench and the Venturi scrubber (see Section S4), sampling was carried out at times outside the stationary operating conditions. pH, electrical conductivity and concentrations of TIC, TOC and several trace components were measured under ambient conditions using the standards given in Table S8. Specifically, concentrations were determined to capture data on dissolved and dissociated gases as well as of intermediates and by-products.

3.2. Stationary conditions

The periods of time with approximately stationary conditions were defined subsequent to the campaign using (i) the evaluation of the time histories of the measurement data (see Section S6) and the elemental balancing data and (ii) lead times of at least 6 h. The measurement data of each selected period of time was time-averaged over 45-60 minutes and transferred to the programme with the balancing model (see Section 3.4) and the equilibrium model (see Section 3.5).

3.3. Boundaries and property methods

The boundaries of the overall system and the inner reactor chamber are marked with red and yellow lines in Fig. 1. The gas streams passing the boundaries are described using the Peng-Robinson equation of state and the property methods and data (COMBUST and PURE40) adopted from Aspen Properties [62]. The pure steam streams are modelled using IAPWS-97 [71]. The detailed compositions of oxygen, nitrogen and natural gas are described using the data of the gas suppliers, that is listed in Tables S1-S3. Specifically,

16

the composition of natural gas was obtained from the monthly averaged data of Open Grid Europe for the period of the campaign with the bioliq EFG experiments V82, V83, V84 and V85. The mass fractions $\boldsymbol{w}_{\mathrm{ng}}$ of major natural gas components are given in Table 2.

Table 2: Mass fractions $\boldsymbol{w}_{\mathrm{ng}}$ of major natural gas components in detailed composition based on the monthly averaged data reported by Open Grid Europe and simplified composition.

Natural gas	$w_{\mathrm{CH_4,ng}}$	$w_{\mathrm{C_2H_6,ng}}$	$w_{\mathrm{CO_2,ng}}$	$w_{\mathrm{N_2,ng}}$
Detailed	0.8265	0.0985	0.0449	0.0137
Simplified	0.9414	–	0.0449	0.0137

Furthermore, the ethylene glycol stream is defined using its theoretical composition, and the beach wood pyrolysis oil stream is accounted for using (i) the results of the proximate, ultimate and heating value analyses and (ii) the correlation of Kirov [72] for heat capacity and physical enthalpy. The further material properties of the ethylene glycol stream are determined using the property methods and data (COMBUST and PURE40) of Aspen Properties [62].

3.4. Balancing model

The balancing model is applied for the evaluation of bioliq EFG experiments with emphasis on process quality and efficiency. It comprises elemental balances as well as energy balances of the inner reactor chamber and the cooling screen (see Figs. S1 and S2).

3.4.1. Elemental balances

The elemental balances are used to derive the balanced gas composition at position B in mole fractions $\boldsymbol{x}_{\mathrm{bal,B}}$ from the compositions and flow rates of the feed streams and the dry gas composition at position C in mole fractions $\boldsymbol{x}_{\mathrm{meas,dry,C}}$ and are based on the assumptions described below:

- CH_4, CO, CO_2, H_2, N_2, H_2S and HCl are accounted for as gas species only, while neglecting gas species such as NH_3 and HCN.

- CH_4, CO, CO_2, H_2 and N_2 are taken into account using the measurement data from position C.

- Fuel sulphur and fuel chlorine are completely volatised and converted to H_2S and HCl at position B.

- Carbon which is not accounted for by the measured gas species concentrations of CH_4, CO and CO_2 is described as lost carbon.

- Undetected hydrogen is assumed as lost atomic hydrogen and described using a pre-defined atomic hydrogen/carbon loss ratio.

- The mineral slurry components are assumed to be inert.

- The loss of dissolved and dissociated CO_2 with the discharged waste water is accounted for while solutions and dissociations of other gas species are neglected due to their low gas solubilities.

The elemental balances are in particular applied to calculate (i) the molar flow rate of the dry gas at position C $\dot{n}_{\text{gas,dry,bal,C}}$, (ii) the balanced molar flow rate of H_2O at position B $\dot{n}_{\text{H}_2\text{O,bal,B}}$, (iii) the molar flow rate of CO_2 in the waste water stream $\dot{n}_{\text{CO}_2,\text{quench}}$ and (iv) the molar flow rate of lost carbon $\dot{n}_{\text{C,loss}}$. Thereby, the elemental balances do not require the mass flow rates of fresh water to quench and the Venturi scrubber and of waste water from the quench

and the Venturi scrubber. The elemental balance equations are given by

$$\dot{n}_{\mathrm{C,A}} = \left(x_{\mathrm{CH_4,meas,dry,C}} + x_{\mathrm{CO,meas,dry,C}} + x_{\mathrm{CO_2,meas,dry,C}}\right)$$
$$\cdot \dot{n}_{\mathrm{gas,dry,bal,C}} + \dot{n}_{\mathrm{CO_2,quench}} + \dot{n}_{\mathrm{C,loss}} \,, \tag{2}$$

$$\dot{n}_{\mathrm{H,A}} = \left(4\,x_{\mathrm{CH_4,meas,dry,C}} + 2\,x_{\mathrm{H_2,meas,dry,C}} + 2\,x_{\mathrm{H_2S,calc,dry,C}}\right.$$
$$\left. + x_{\mathrm{HCl,calc,dry,C}}\right)\dot{n}_{\mathrm{gas,dry,bal,C}} + 2\,\dot{n}_{\mathrm{H_2O,bal,B}}$$
$$+ \mathrm{HCR_{loss}}\,\dot{n}_{\mathrm{C,loss}} \,, \tag{3}$$

$$\dot{n}_{\mathrm{O,A}} = \left(x_{\mathrm{CO,meas,dry,C}} + 2\,x_{\mathrm{CO_2,meas,dry,C}}\right)\dot{n}_{\mathrm{gas,dry,bal,C}} + \dot{n}_{\mathrm{H_2O,bal,B}}$$
$$+ 2\,\dot{n}_{\mathrm{CO_2,quench}} \,, \tag{4}$$

$$\dot{n}_{\mathrm{N,A}} = 2\,x_{\mathrm{N_2,meas,dry,C}}\,\dot{n}_{\mathrm{gas,dry,bal,C}} - 2\,\dot{n}_{\mathrm{N_2,csp}} \,, \tag{5}$$

$$\dot{n}_{\mathrm{S,A}} = x_{\mathrm{H_2S,calc,dry,C}}\,\dot{n}_{\mathrm{gas,dry,bal,C}} \,, \tag{6}$$

$$\dot{n}_{\mathrm{Cl,A}} = x_{\mathrm{HCl,calc,dry,C}}\,\dot{n}_{\mathrm{gas,dry,bal,C}} \,, \tag{7}$$

where $\dot{n}_{\mathrm{C,A}}$, $\dot{n}_{\mathrm{H,A}}$, $\dot{n}_{\mathrm{O,A}}$, $\dot{n}_{\mathrm{N,A}}$, $\dot{n}_{\mathrm{S,A}}$ and $\dot{n}_{\mathrm{Cl,A}}$ are the molar flow rates of C, H, O, N, S and Cl at position A; $x_{\mathrm{CH_4,meas,dry,C}}$, $x_{\mathrm{CO,meas,dry,C}}$, $x_{\mathrm{CO_2,meas,dry,C}}$, $x_{\mathrm{H_2,meas,dry,C}}$ and $x_{\mathrm{N_2,meas,dry,C}}$ are the measured dry gas species mole fractions of $\mathrm{CH_4}$, CO, $\mathrm{CO_2}$, $\mathrm{H_2}$ and $\mathrm{N_2}$ at position C; $x_{\mathrm{H_2S,calc,dry,C}}$ and $x_{\mathrm{HCl,calc,dry,C}}$ are the calculated dry gas species mole fractions of $\mathrm{H_2S}$ and HCl at position C; $\mathrm{HCR_{loss}}$ is the atomic hydrogen/carbon loss ratio; $\dot{n}_{\mathrm{N_2,csp}}$ is the molar flow rate of $\mathrm{N_2}$ which is used for purging of the cooling screen and is conveyed to the synthesis gas in the quench. The atomic hydrogen/carbon loss ratio $\mathrm{HCR_{loss}}$ is assumed to be zero (i. e. soot/pure carbon) in this study. The balanced gas molar flow rate at position B $\dot{n}_{\mathrm{gas,bal,B}}$ is given by

$$\dot{n}_{\mathrm{gas,bal,B}} = \dot{n}_{\mathrm{gas,dry,bal,C}} - \dot{n}_{\mathrm{N_2,csp}} + \dot{n}_{\mathrm{CO_2,quench}} + \dot{n}_{\mathrm{H_2O,bal,B}} \,. \tag{8}$$

The balanced gas composition at position B in mole fractions $\boldsymbol{x}_{\mathrm{bal,B}} = (x_{i,\mathrm{bal,B}})$ is finally defined by

$$x_{i,\mathrm{bal,B}} = \begin{cases} \dfrac{\dot{n}_{\mathrm{H_2O,bal,B}}}{\dot{n}_{\mathrm{gas,bal,B}}} \,, & \text{if } i = \mathrm{H_2O} \\[2ex] \dfrac{x_{\mathrm{CO_2,meas,dry,C}}\,\dot{n}_{\mathrm{gas,bal,dry,C}} + \dot{n}_{\mathrm{CO_2,quench}}}{\dot{n}_{\mathrm{gas,bal,B}}} \,, & \text{if } i = \mathrm{CO_2} \\[2ex] \dfrac{x_{i,\mathrm{gas,dry,C}}\,\dot{n}_{\mathrm{gas,bal,dry,C}}}{\dot{n}_{\mathrm{bal,B}}} \,, & \text{else} \end{cases} \tag{9}$$

3.4.2. Energy balance of the inner reactor chamber

The energy balance of the inner reactor chamber is used to determine the balanced temperature at position B $T_{\text{bal,B}}$ from the chemical and physical enthalpy flow rates of the measured input and the balanced output streams as well as the heat extraction of the cooling screen (see Section 3.4.3).

3.4.3. Energy balances of the cooling screen

The energy balances of the cooling screen are used to determine the heat extraction neglecting peripheral heat losses of the cooling screen and the cooling water pipes. The heat extraction is used as an input for both the balancing model and the equilibrium model and provides the main validation data for CFD models. The calculation steps for the averaged values and the uncertainties of the heat flow rates $\dot{\boldsymbol{Q}}$ and heat fluxes $\dot{\boldsymbol{q}}$ are described below.

The heat flow rates $\dot{\boldsymbol{Q}} = (Q_i)$ of the eight cooling circuits (see Fig. 2) are given by

$$\dot{Q}_i = \frac{\dot{m}_{i,\text{in}} + \dot{m}_{i,\text{out}}}{2} \left(\hat{H}_{\text{water}}\bigg|_{T_{i,\text{out}},p_{i,\text{out}}} - \hat{H}_{\text{water}}\bigg|_{T_{i,\text{in}},p_{i,\text{in}}} \right) , \tag{10}$$

where $\dot{m}_{i,\text{in}}$ is the mass flow rate at inlet and $\dot{m}_{i,\text{out}}$ is the mass flow rate at outlet, each of cooling circuit i, and $\hat{H}_{\text{water}}$ is the specific enthalpy of water according to IAPWS-97 [71]. Furthermore, $T_{i,\text{out}}$ is the temperature at outlet, $p_{i,\text{out}}$ is the pressure at outlet, $T_{i,\text{in}}$ is the temperature at inlet and $p_{i,\text{in}}$ is the pressure at inlet, each of cooling circuit i. Averaging of the mass flow rates of the cooling circuits is applied due to slightly deviating measurement data from the calibrated mass flow controllers at inlet and outlet.

Furthermore, the top heat flow rate $\dot{Q}_{\text{top}}$ and the total heat flow rate $\dot{Q}_{\text{tot}}$ are defined by

$$\dot{Q}_{\text{top}} = \dot{Q}_{\text{ST}} + \dot{Q}_{\text{sb}} + \dot{Q}_{\text{ngb}} , \tag{11}$$

$$\dot{Q}_{\text{tot}} = \dot{Q}_{\text{top}} + \sum_{i=1}^{5} \dot{Q}_{\text{S}i} , \tag{12}$$

where $\dot{Q}_{\text{ST}}$, $\dot{Q}_{\text{sb}}$, $\dot{Q}_{\text{ngb}}$ and $\dot{Q}_{\text{S}i}$ are the heat flow rates extracted at segment top, the slurry burner, the natural gas burner and segment i, respectively. The

total heat flow rate $\dot{Q}_{\text{tot}}$ provides the heat extraction used to determine the balanced temperature at position B $T_{\text{bal,B}}$ within the balancing model and the equilibrium temperature at position B $T_{\text{eq,B}}$ within the equilibrium model.

The heat fluxes $\dot{\boldsymbol{q}} = (\dot{q}_i)$ are determined by

$$\dot{q}_i = \frac{\dot{Q}_i}{A_{\text{s},i}} , \tag{13}$$

where $i =$ S1, S2, S3, S4, S5, ST and $A_{\text{s},i}$ is the surface area of segment i (see Table S20).

The uncertainties in the heat flow rates $\boldsymbol{\Delta\dot{Q}} = \left(\Delta\dot{Q}_i\right)$ and the heat fluxes $\boldsymbol{\Delta\dot{q}} = (\Delta\dot{q}_i)$ are defined based on Gaussian uncertainty propagation and are determined by

$$\begin{aligned} \Delta\dot{Q}_i = \Bigg(& \left(\Delta\dot{m}_{i,\text{in}}\,\hat{H}_{i,\text{in}}\right)^2 + \left(\dot{m}_{i,\text{in}}\,\Delta\hat{H}_{i,\text{in}}\right)^2 \\ & + \left(\Delta\dot{m}_{i,\text{out}}\,\hat{H}_{i,\text{out}}\right)^2 + \left(\dot{m}_{i,\text{out}}\,\Delta\hat{H}_{i,\text{out}}\right)^2 \Bigg)^{1/2} , \end{aligned} \tag{14}$$

$$\Delta\dot{q}_i = \frac{\Delta\dot{Q}_i}{A_{\text{s},i}} , \tag{15}$$

where $\Delta\dot{m}_{i,\text{in}}$, $\Delta\dot{m}_{i,\text{out}}$, $\Delta\hat{H}_{i,\text{in}}$ and $\Delta\hat{H}_{i,\text{out}}$ are the standard deviations of the respective variables.

3.5. Equilibrium model

The equilibrium model is used for the design, analysis and evaluation of bioliq EFG experiments and the verification of the balancing predictions. The model includes all process units within the system boundary (marked with a red line in Fig. 1). Apart from elemental and energy balances, it is based on equilibrium calculations in particular to determine the equilibrium temperature at position B $T_{\text{eq,B}}$, the equilibrium composition at position B in mole fractions $\boldsymbol{x}_{\text{eq,B}}$ and the equilibrium-derived composition at position C in mole fractions $\boldsymbol{x}_{\text{eq,C}}$. The model only relies on the chemical slurry properties, the total heat extraction, the data of the input streams and the assumptions described below:

21

- CH_4, CO, CO_2, H_2, H_2O, O_2, N_2, H_2S, HCl, NH_3, HCN, Ar, C_2H_2, C_2H_4, C_2H_6, $C_2H_6O_2$, C_3H_8, C_6H_6, $C_{10}H_8$, $NaOH$, S, Cl_2, SO_2, SO_3 and $C(s)$ are accounted for as species.

- The mineral slurry components are assumed to be inert.

- The total heat extraction is given by the heat removal through the cooling circuits. Peripheral heat losses are neglected.

- The synthesis gas at position C is saturated with water vapour corresponding to the measured gas temperature at position C.

The equilibrium model was implemented using unit operations of Aspen Plus [73] and the property methods and data of Aspen Properties [62] (see Section 3.3). The equilibrium calculations are based on the minimisation of the Gibbs energy, whereas quench, Venturi scrubber and separators are described using mixers and flash separators and neglecting chemical reactions.

The equilibrium model can be applied assuming either a restricted equilibrium or a complete equilibrium. A restricted equilibrium is incorporated using inert predefined streams of solid carbon or hydrocarbons to account for by-products and is typically used to reproduce experimental data or to generate scale-up data. In contrast, a complete equilibrium is used to derive information regarding maximum conversion and typically performs well for highly reactive fuels, ideal operating conditions and temperatures above $1700\,K$ (see [35, 38, 39]). In this study, the equilibrium model was utilised assuming a complete equilibrium.

3.6. Characteristic temperatures

The fuel reactivity, the slag deposition and the construction materials of the inner reactor chamber constrain the gas temperature in the inner reactor chamber. The gas temperature is therefore the most important target parameter for the design and scale-up of entrained flow gasification processes using simulation models. As measurements of gas temperatures inside the

inner reactor chamber of the bioliq EFG have not been performed yet, special attention was given in this study to the reliable determination of the gas temperature at position B $T_{\text{gas,B}}$. With the water-gas shift temperature $T_{\text{WGS,B}}$ (see Section 2.2), the balanced temperature $T_{\text{bal,B}}$ (see Section 3.4) and the equilibrium temperature $T_{\text{eq,B}}$ (see Section 3.5), three different characteristic temperatures were introduced for position B. These temperatures can be connected to each other and to the gas temperature at position B $T_{\text{gas,B}}$ in the boundary cases described below:

- If a complete equilibrium is expected for position B due to a high operating temperature and a high fuel reactivity and if peripheral heat losses can be neglected, the gas temperature $T_{\text{gas,B}}$ is close to the equilibrium temperature $T_{\text{eq,B}}$ and the balanced temperature $T_{\text{bal,B}}$.

- If a complete equilibrium is not achieved and intermediates occur due to lower operating temperatures or a lower fuel reactivity, the gas temperature $T_{\text{gas,B}}$ and the balanced temperature $T_{\text{bal,B}}$ are above the equilibrium temperature $T_{\text{eq,B}}$ (see Section 2.1).

- If peripheral heat losses cannot be both neglected and accounted for, the equilibrium temperature $T_{\text{eq,B}}$ and the balanced temperature $T_{\text{bal,B}}$ are higher than the gas temperature $T_{\text{gas,B}}$.

- If the gas temperature $T_{\text{gas,B}}$ is below the freezing temperature of the WGS reaction (see Section 2.2) and a partial WGS equilibrium is expected for position B, the WGS temperature $T_{\text{WGS,B}}$ is close to the gas temperature $T_{\text{gas,B}}$. The WGS temperature $T_{\text{WGS,B}}$ reflects peripheral heat losses because it is not affected by the energy balances of the inner reactor chamber and the cooling screen.

- If the gas temperature $T_{\text{gas,B}}$ is above the freezing temperature of the WGS reaction, the WGS temperature $T_{\text{WGS,B}}$ drops to the freezing temperature corresponding to the cooling rate in the quench (see Section 2.2).

23

The boundary cases assume accurate and reliable input data. Specifically, the accuracy of the chemical fuel data strongly affects the evaluation of the three characteristic temperatures (see Section 4.3.3).

3.7. Characteristic parameters

Four characteristic parameters were used in this study to evaluate the bioliq EFG experiments, namely: the carbon conversion CC, the cold gas efficiency CGE, the synthesis gas yield Y and the loss of dissolved and dissociated CO_2 with the discharged waste water CO2L. Specifically, the carbon conversion, the cold gas efficiency and the synthesis gas yield at well-defined process temperatures enable the quantitative evaluation of entrained flow gasification experiments and thus the fuel-specific optimisation of process operating parameters for the design and scale-up of entrained flow gasification processes.

3.7.1. Carbon conversion

The carbon conversion CC as a performance parameter for fuel reactivity is defined as the ratio of the carbon found in the gas phase to the carbon fed into the entrained flow gasifier [61]. In this study, balanced carbon conversions CC_{bal} and equilibrium carbon conversions CC_{eq} were derived alongside carbon conversions based on the ash tracer method CC_{at} [74], carbon conversions based on the waste water method CC_{ww} [20, 21] and carbon conversions based on both the waste water method and the ash tracer method CC_{ww+at}. The balanced carbon conversion CC_{bal} and the equilibrium carbon conversion CC_{eq} are defined by

$$CC_{bal} = \frac{\dot{n}_{gas,bal,B}}{\dot{n}_{C,A}} \sum_{i=CH_4,CO,CO_2} x_{i,bal,B} , \tag{16}$$

$$CC_{eq} = \frac{\dot{n}_{gas,eq,B}}{\dot{n}_{C,A}} \sum_{i=CH_4,CO,CO_2} x_{i,eq,B} , \tag{17}$$

where $\dot{n}_{gas,bal,B}$ is the balanced gas molar flow rate at position B and $\dot{n}_{gas,eq,B}$ is the equilibrium gas molar flow rate at position B. The balanced carbon

conversion CC_{bal} and the equilibrium carbon conversion CC_{eq} thus account for carbon through CH_4, CO and CO_2 only while neglecting higher gaseous hydrocarbons.

The carbon conversion based on the ash tracer method CC_{at} assumes that incompletely converted carbon (carbonaceous residues, soot) deposits on the surfaces of ash particles and slag and is given by [74]

$$CC_{at} = 1 - \frac{w_{C,slag} \, w_{ash,slurry}}{(1 - w_{C,slag}) \, w_{C,slurry}} \, , \tag{18}$$

where $w_{C,slag}$ is the carbon content of the slag, $w_{C,slurry}$ is the carbon content of the slurry and $w_{ash,slurry}$ is the ash content of the slurry (see Sections 3.1.2 and 4.1.1). The carbon conversion based on the ash tracer method CC_{at} thus neglects higher gaseous hydrocarbons and carbon losses due to solution in waste water.

The carbon conversion based on the waste water method CC_{ww} assumes that incompletely converted carbon (carbonaceous residues, soot) can be found as organic carbon in the waste water and is defined by [20, 21]

$$CC_{ww} = 1 - \frac{1}{w_{C,slurry} \, \dot{m}_{slurry}} \sum_{i=quench,scrubber} c_{TOC,ww,i} \, \dot{m}_{ww,i} \, , \tag{19}$$

where $c_{TOC,ww,quench}$ and $c_{TOC,ww,scrubber}$ are the mass concentrations of TOC in the waste water streams of the quench and the Venturi scrubber (see Section 3.1.2). The carbon conversion based on the waste water method CC_{ww} thus does not account for higher gaseous hydrocarbons and carbon losses through the slag flow.

The carbon conversion based on both the waste water method and the ash tracer method CC_{ww+at} relies on the assumption of both the waste water method and the ash tracer method and is given by

$$CC_{ww+at} = CC_{ww} + CC_{at} - 1 \, . \tag{20}$$

In summary, all approaches for the calculation of carbon conversion neglect higher hydrocarbons, which typically leads to higher carbon conversions CC_{at}, CC_{ww} and CC_{ww+at} and lower carbon conversions CC_{bal} and CC_{eq}.

3.7.2. Cold gas efficiency

The cold gas efficiency CGE as a performance parameter for process efficiency is defined using the heating value of the slurry and the heating values of the combustible species detected in the synthesis gas [16]. In this study, the balanced cold gas efficiency CGE_{bal} and the equilibrium cold gas efficiency CGE_{eq} are given by

$$CGE_{bal} = \frac{1}{\dot{m}_{slurry,A} \, LHV_{slurry}} \sum_{i=CH_4,CO,H_2} \dot{m}_{i,bal,B} \, LHV_i \,, \tag{21}$$

$$CGE_{eq} = \frac{1}{\dot{m}_{slurry,A} \, LHV_{slurry}} \sum_{i=CH_4,CO,H_2} \dot{m}_{i,eq,B} \, LHV_i \,, \tag{22}$$

where $\dot{m}_{slurry,A}$ is the mass flow rate of the slurry at position A, $\dot{m}_{i,bal,B}$ is the balanced mass flow rate of species i at position B, $\dot{m}_{i,eq,B}$ is the equilibrium mass flow rate of species i at position B, LHV_{slurry} is the lower heating value of the slurry and LHV_i is the lower heating value of species i.

3.7.3. Yield

The synthesis gas yield, as a performance parameter for the optimisation of entrained flow gasification processes coupled with synthesis gas applications [60], is defined as the amount of substance of CO and H_2 per mass of fuel [60]. In this study, the balanced yield Y_{bal} and the equilibrium yield Y_{eq} are given by

$$Y_{bal} = \frac{1}{\dot{m}_{slurry,A}}, \sum_{i=CO,H_2} \dot{n}_{i,bal,B} \,, \tag{23}$$

$$Y_{eq} = \frac{1}{\dot{m}_{slurry,A}}, \sum_{i=CO,H_2} \dot{n}_{i,eq,B} \,, \tag{24}$$

where $\dot{n}_{i,bal,B}$ is the balanced molar flow rate of species i at position B and $\dot{n}_{i,eq,B}$ is the equilibrium molar flow rate of species i at position B.

3.7.4. Loss of dissolved and dissociated CO_2

The loss of dissolved and dissociated CO_2 with the discharged waste water CO2L is defined by

$$CO2L = \frac{\dot{n}_{CO_2,quench}}{\dot{n}_{CO_2,bal,B}} \,, \tag{25}$$

26

where $\dot{n}_{CO_2,\text{quench}}$ is the molar flow rate of dissolved and dissociated CO_2 and $\dot{n}_{CO_2,\text{bal,B}}$ is the balanced molar flow rate of CO_2 at position B.

4. Results

This section presents and discusses the results of the measurements, the analyses and the balancing and equilibrium calculations for the bioliq EFG experiments V82, V83, V84 and V85 in combination with sensitivity analyses.

4.1. Experimental data

The experimental data was used to evaluate the stationarity of the bioliq EFG experiments and to derive input and validation data for both balancing and equilibrium calculations as well as CFD simulations.

4.1.1. Chemical slurry properties

The measured compositions and heating values of the beech wood pyrolysis oil samples are summarised in Tables S9 and S10. Furthermore, higher heating values based on the Boie correlation [75] and ratios of the higher heating value based on the Boie correlation [75] to the measured higher heating values (Boie ratios) are given in Table S10. The Boie ratios show that the reported compositions and heating values are clearly scattered. Following previous recommendations [60], the analysis results with the best agreement of calculated and measured higher heating values were selected for the further evaluation (see Section 4.3.3).

Furthermore, the chemical slurry properties were determined using the ash/slurry mass flow rate ratios (see Table 1), the theoretical values of (pure) ethylene glycol in the case of the bioliq EFG experiments V82, V83 and V84 and the selected chemical analysis results of the beech wood pyrolysis oil in the case of the bioliq EFG experiment V85. Alongside the molar H/C ratios HCR_{slurry} and the minimum specific oxygen demands $SMOD_{\text{slurry}}$, the compositions and the higher heating values are listed in Tables 3 and 4. The technical slurry used in the bioliq EFG experiment V85 is thus

27

characterised by an elevated higher heating value compared to the surrogate slurries in the bioliq EFG experiments V82, V83 and V84, which corresponds to a lower atomic H/C ratio $\mathrm{HCR_{slurry}}$ and a higher specific minimum oxygen demand $\mathrm{SMOD_{slurry}}$. Furthermore, higher heating values based on the slurry compositions and the Boie correlation [75] are given in Table 4 demonstrating good agreement with the theoretical values.

Table 3: Characteristic slurry data: compositions in mass fractions (as-received) based on the theoretical ethylene glycol composition in the case of the bioliq EFG experiments V82, V83 and V84 or on the chemical analysis results in the case of the bioliq EFG experiment V85.

Experiment	$w_{\mathrm{C,slurry}}$	$w_{\mathrm{H,slurry}}$	$w_{\mathrm{O,slurry}}$	$w_{\mathrm{N,slurry}}$	$w_{\mathrm{S,slurry}}$	$w_{\mathrm{Cl,slurry}}$	$w_{\mathrm{ash,slurry}}$	$w_{\mathrm{H_2O,slurry}}$
V82	0.3696	0.0931	0.4923	–	–	–	0.0450	–
V83	0.3696	0.0931	0.4923	–	–	–	0.0450	–
V84	0.3522	0.0887	0.4691	–	–	–	0.0900	–
V85	0.5549	0.0609	0.2849	0.0013	0.0003	0.0001	0.0460	0.0516

Table 4: Characteristic slurry data: higher heating values (as received) $\mathrm{HHV_{slurry,asr}}$ based on the theoretical value in the case of the bioliq EFG experiments V82, V83 and V84 or on the chemical analysis results in the case of the bioliq EFG experiment V85, higher heating values based on the Boie correlation (as received) $\mathrm{HHV_{Boie,slurry,asr}}$, molar H/C ratios $\mathrm{HCR_{slurry}}$ and specific minimum oxygen demands $\mathrm{SMOD_{slurry}}$.

Experiment	$\dfrac{\mathrm{HHV_{slurry,asr}}}{\mathrm{MJ/kg}}$	$\dfrac{\mathrm{HHV_{Boie,slurry,asr}}}{\mathrm{MJ/kg}}$	$\dfrac{\mathrm{HCR_{slurry}}}{\mathrm{mol/mol}}$	$\dfrac{\mathrm{SMOD_{slurry}}}{\mathrm{kg/kg}}$
V82	18.227	18.322	3.000	1.231
V83	18.227	18.322	3.000	1.231
V84	17.368	17.458	3.000	1.173
V85	23.397	23.309	1.308	1.677

4.1.2. Feed streams

The averaged mass flow rates and the corresponding enthalpy flow rates of the feed streams at position A are given in Tables 5 and S11. Lower mass flow rates of liquid fuel were used in the bioliq EFG experiments V84 and V85 compared to the bioliq EFG experiments V82 and V83 in order to operate the bioliq EFG reactor within the limits of the mass flow rate of slurry and the thermal input, respectively. Furthermore, high mass flow rates of N_2 were applied in each of the four bioliq EFG experiments for purging purposes. In particular, the use of a camera system for flame observation required increased mass flow rates of N_2 in the bioliq EFG experiments V83, V84 and V85.

Table 5: Feed data at position A: mass flow rates of liquid fuel $\dot{m}_{\text{liquid fuel,A}}$, mass flow rates of ash $\dot{m}_{\text{ash,A}}$, mass flow rates of natural gas $\dot{m}_{\text{ng,A}}$, mass flow rates of steam $\dot{m}_{\text{steam,A}}$, mass flow rates of O_2 $\dot{m}_{O_2,A}$ and mass flow rates of N_2 $\dot{m}_{N_2,A}$ based on measurements.

Experiment	$\dot{m}_{\text{liquid fuel,A}}$ kg/h	$\dot{m}_{\text{ash,A}}$ kg/h	$\dot{m}_{\text{ng,A}}$ kg/h	$\dot{m}_{\text{steam,A}}$ kg/h	$\dot{m}_{O_2,A}$ kg/h	$\dot{m}_{N_2,A}$ kg/h
V82	744.73	35.09	40.0	299.57	615.73	174.88
V83	740.39	34.89	40.0	294.56	576.85	189.19
V84	703.90	69.62	40.0	297.01	605.83	202.90
V85	691.26	32.57	40.0	290.11	635.86	207.09

4.1.3. Dry gas species concentrations

The averaged dry gas species concentrations at position C in mole fractions are given in Table 6. The gas species mole fraction of H_2 at position C $x_{H_2,\text{meas,dry,C}}$ was 29-32 % while the gas species mole fraction of CO at position C $x_{\text{CO,meas,dry,C}}$ was significantly higher in the bioliq EFG experiment V85 than in the bioliq EFG experiments V82, V83 and V84 since, due to the higher carbon content and the elevated higher heating value of the beech wood pyrolysis oil, a lower stoichiometric ratio λ (see Table 1) was applied in the bioliq EFG experiment V85 to keep the gas temperatures similar to the bioliq EFG experiments V82, V83 and V84.

Furthermore, the dry gas species mole fraction of CH_4 at position C $x_{CH_4,\text{meas,dry,C}}$ was lower in the bioliq EFG experiments V82 and V84 than in the bioliq EFG experiment V83 which indicates lower gas temperatures in the bioliq EFG experiment V83. Note that this conclusion cannot be transferred to the bioliq EFG experiment V85 due to the use of beech wood pyrolysis oil instead of ethylene glycol (i.e. due to the different molar H/C ratio $\text{HCR}_{\text{slurry}}$).

Table 6: Dry gas species concentrations at position C in mole fractions $\boldsymbol{x}_{\text{meas,dry,C}}$ based on gas chromatography measurements.

Experiment	$x_{CH_4,\text{meas,dry,C}}$	$x_{CO,\text{meas,dry,C}}$	$x_{CO_2,\text{meas,dry,C}}$	$x_{H_2,\text{meas,dry,C}}$	$x_{N_2,\text{meas,dry,C}}$	$\dfrac{x_{H_2,\text{meas,dry,C}}}{x_{CO,\text{meas,dry,C}}}$
V82	0.0009	0.2763	0.2372	0.3230	0.1626	1.17
V83	0.0077	0.2700	0.2130	0.3221	0.1872	1.19
V84	0.0016	0.2680	0.2357	0.2972	0.1975	1.11
V85	0.0046	0.3807	0.1699	0.2960	0.1488	0.78

4.1.4. Refractory temperatures

The refractory temperatures are given in Tables S12 and S13 and are shown for the bioliq EFG experiment V85 in Fig. 3. First of all, it should be emphasised that (i) the refractory temperatures strongly depend on the gas temperature distribution, the slag deposition and the refractory/cooling screen construction (see Section S6) and (ii) the gas temperature distribution and the thickness of the slag deposition in the upper part of the inner chamber strongly depend on the stationary flame shape. A slightly imperfect axisymmetric orientation of the stationary flame, a slightly imperfect uniform refractory coating or a non-uniform slag deposition at the junctions of cylindrical and conical segments strongly affect the refractory temperatures. Therefore, the refractory temperatures measured using the uppermost opposite thermocouples T1 and T2 and the lowermost opposite thermocouples T9 and T10 deviate by up to 75 K. In contrast, the thermocouples T3 and T4, T5 and T6 and T7 and T8 determined quite similar temperatures in each of the four bioliq EFG experiments. Thus, the measurements at positions T3 and T4,

T5 and T6 and T7 and T8 provided meaningful validation data for slag flow models.

4.1.5. Chemical slag properties

The carbon content of the slag samples from the bioliq EFG experiments V82, V83 and V84 was less than 0.1% (i.e. below the detection limit), whereas the carbon content of the slag sample from the bioliq EFG experiment V85 was 0.4%. The sulphur and chlorine contents of the slag samples were also below the detection limit, which is in agreement with the sulphur and chlorine contents of the respective fuels. Furthermore, visual observations of the slag deposition subsequent to each bioliq EFG experiment [70] indicated low carbon content for the bioliq EFG experiments V82, V83 and V84. Thus, the slag analysis data is in agreement with the visual observations and provides reasonable results.

4.1.6. Waste water properties

The pH, the electrical conductivity and the concentrations of major species in the waste water of the quench are given in Table S14 while the concentrations of TIC and TOC in the waste water of the Venturi scrubber are listed in Table S15. Dissolved carbon was mainly found in the form of formate, TOC and TIC, and dissolved nitrogen was found in the form of ammoniacal nitrogen. Furthermore, this data requires a careful analysis. Gases with high solubilities such as CO_2 and NH_3 accumulate in the quench water over long operating times. The dissolved gases dissociate and enhance further chemical reactions in the quench water leading in particular to the formation of formate. Furthermore, dissolved and dissociated gases that are unstable in solution, such as CO_2, degas at depressurisation. Therefore, the measured data only provides snapshots of the waste water properties at the respective times and does not reflect the properties prevailing in the quench water under the stationary pressurised operating conditions. Specifically, the solution and dissociation of CO_2 cannot be quantified by waste water analyses under ambient conditions

31

(see Section S5.2). Further conclusions are summarised below:

1. The concentration of ammoniacal nitrogen was approximately five times higher in the bioliq EFG experiment V85 than in the bioliq EFG experiments V82, V83 and V84. As this was due to either the higher nitrogen content of pyrolysis oil or the longer operating time, the measured concentration cannot be linked to the concentration of ammonia in the synthesis gas.

2. The concentrations of sodium and formate were higher in the bioliq EFG experiments V83 and V85 than in the bioliq EFG experiments V82 and V84 corresponding to the higher pH. The higher concentrations were caused by residues of NaOH dosages.

3. The pH and the concentrations of formate, sodium and ammoniacal nitrogen are closely related to the electrical conductivity κ, whereas this applies less to the concentration of TIC (see Fig. 4). Furthermore, the concentration of formate corresponds to the TOC concentration, which shows that formate was the only organic carbon compound present.

4.2. Balancing and equilibrium data

The balancing and equilibrium models were used to determine and to verify the synthesis gas condition at position B, to reflect the changes in the synthesis gas composition between the positions B and C and to obtain characteristic parameters for design and scale-up.

4.2.1. Elemental balancing data

The balanced gas compositions at position B in mole fractions $\boldsymbol{x}_{\mathrm{bal,B}}$ and the corresponding WGS temperatures at position B $T_{\mathrm{WGS,B}}$, the balanced carbon conversions $\mathrm{CC}_{\mathrm{bal}}$ and the CO_2 losses CO2L are given in Table 7.

Table 7: Balanced compositions at position B in mole fractions $\boldsymbol{x}_{\mathrm{bal,B}}$, WGS temperatures at position B $T_{\mathrm{WGS,B}}$, balanced carbon conversions $\mathrm{CC}_{\mathrm{bal}}$ and balanced $\mathrm{CO_2}$ losses CO2L.

Experiment	$x_{\mathrm{CH_4,bal,B}}$	$x_{\mathrm{CO,bal,B}}$	$x_{\mathrm{CO_2,bal,B}}$	$x_{\mathrm{H_2,bal,B}}$	$x_{\mathrm{H_2O,bal,B}}$	$x_{\mathrm{N_2,bal,B}}$	$\dfrac{T_{\mathrm{WGS,B}}}{\mathrm{K}}$	$\dfrac{\mathrm{CC_{bal}}}{\%}$	$\dfrac{\mathrm{CO2L}}{\%}$
V82	0.00053	0.1567	0.1354	0.1835	0.4533	0.0708	1537	99.4	0.7
V83	0.00441	0.1550	0.1296	0.1849	0.4484	0.0777	1546	97.2	5.7
V84	0.00085	0.1406	0.1354	0.1559	0.4819	0.0854	1617	95.1	8.7
V85	0.00314	0.2629	0.1273	0.2044	0.3136	0.0886	1607	93.4	7.8

The WGS temperatures at position B $T_{\mathrm{WGS,B}}$ are accordingly between 1537 K and 1617 K. These temperatures provide good estimates for the gas temperatures at position B $T_{\mathrm{gas,B}}$ as freezing temperatures above 1650 K are expected for the operating and process conditions (see also Section 2.2).

The balanced gas species mole fraction of $\mathrm{H_2O}$ at position B $x_{\mathrm{H_2O,bal,B}}$ is significantly lower in the bioliq EFG experiment V85 than in the bioliq EFG experiments V82, V83 and V84. This is because of the different slurry compositions (see the molar H/C ratios $\mathrm{HCR}_{\mathrm{slurry}}$ in Table 4).

The balanced carbon conversions $\mathrm{CC}_{\mathrm{bal}}$ are significantly below 100 % for the bioliq EFG experiments V83, V84 and V85. Recalling that the analyses did not detect significant amounts of carbon residues in both the slag samples and the waste water samples (see Sections 4.1.5 and 4.1.6) and that the balancing model only accounts for $\mathrm{CH_4}$, CO, $\mathrm{CO_2}$ and solid carbon (see Section 3.4), theses results are caused by the assumptions for the higher hydrocarbons (see also Section 4.3.2). However, higher gaseous hydrocarbons were probably produced in the bioliq EFG experiments V82, V83 and V84, while tar and solid residues were likely present in the bioliq EFG experiment V85. Undetected hydrocarbons should therefore be measured in future studies. Furthermore, the decreased carbon conversions in the bioliq EFG experiments V83, V84 and V85 can be attributed to the purging of a camera system (see Section 4.3.1). In addition, the slurry composition combined with the lower stoichiometric ratio λ (see Table 1) has also strongly decreased the carbon conversion for the bioliq EFG experiment V85.

The $\mathrm{CO_2}$ losses CO2L are up to 9 % for the four bioliq EFG experiments.

Specifically, the bioliq EFG experiments V82 is characterised by a CO_2 loss CO2L of 0.7 %, which is in agreement with the equilibrium TIC concentration due to the low ion concentrations (see Section S5.2). In contrast, CO_2 losses CO2L smaller than 0.1 % were derived from the TIC concentrations of the waste water samples. These losses strongly deviate from the balanced CO_2 losses CO2L due to degassing at depressurisation.

4.2.2. Energy balancing data

The balanced temperatures at position B $T_{bal,B}$, the total heat flow rates $\dot{Q}_{tot}$ and the relative heat extractions $\dot{Q}_{tot}/(P_{th,slurry} + P_{th,ng})$ are given in Table 8 while the heat flow rates $\dot{Q}_{S1}$, $\dot{Q}_{S2}$, $\dot{Q}_{S3}$, $\dot{Q}_{S4}$, $\dot{Q}_{S5}$ and $\dot{Q}_{top}$ are listed in Table S16 and the heat fluxes $\dot{q}_{S1}$, $\dot{q}_{S2}$, $\dot{q}_{S3}$, $\dot{q}_{S4}$ and $\dot{q}_{S5}$ are summarised in Table S17. The heat fluxes of the bioliq EFG experiment V85 are shown in Fig. 3.

Table 8: Balanced temperatures at positions B $T_{bal,B}$, total heat extractions $\dot{Q}_{tot}$ and relative total heat extractions $\dot{Q}_{tot}/(P_{th,slurry} + P_{th,ng})$.

Experiment	$\dfrac{T_{bal,B}}{K}$	$\dfrac{\dot{Q}_{tot}}{kW}$	$\dfrac{\dot{Q}_{tot}}{P_{th,slurry} + P_{th,ng}}$
V82	1621	544.51	0.135
V83	1607	445.81	0.111
V84	1667	524.13	0.137
V85	1672	477.83	0.097

The highest total heat extraction was determined for the bioliq EFG experiment V82 which is characterised by the lowest WGS temperature at position B $T_{WGS,B}$, while the second highest total heat extraction was obtained for the bioliq EFG experiment V84 which has the highest WGS temperature at position B $T_{WGS,B}$. Thus, the heat extraction cannot simply be linked with the gas temperature at position B $T_{gas,B}$ as the heat extraction depends in particular on the local gas temperature distribution and the local slag

deposition [70, 76].

Furthermore, the highest segmental heat extraction was obtained for segment 3 (see Fig. 2). This observation is in agreement with the fact that this segment has a rather thin slag deposition, has the largest surface area and is exposed to high gas temperatures similar to the gas temperature at position B $T_{\mathrm{gas,B}}$ [70, 76].

Lower gas temperatures or higher glass contents of the slurry can reduce the heat extraction due to thicker slag deposition (see Sections 4.1.4 and 4.2.4). Therefore, the higher glass input in the bioliq EFG experiment V84 has increased the slag deposition and reduced the heat extraction. Furthermore, less heat was extracted in the bioliq EFG experiment V83 than in the bioliq EFG experiment V82 due to thicker slag deposition [70]. Combined with the incomplete balanced carbon conversion CC_{bal}, the thicker slag deposition led to a slightly higher WGS temperature at position B $T_{\mathrm{WGS,B}}$ despite lower stoichiometry. In summary, the balanced heat extraction data is reasonable and can be used as validation data for CFD models. This applies regardless of the gas conditions in the inner reactor chamber. Specifically, even if equilibrium conditions can be expected for the outlet of the inner reactor chamber (see Section 4.2.4), the balanced heat extractions can still be used for validation.

4.2.3. Equilibrium data

The equilibrium compositions in mole fractions $\boldsymbol{x}_{\mathrm{eq,B}}$ and the equilibrium temperatures $T_{\mathrm{eq,B}}$ at position B are given in Table 9.

Table 9: Equilibrium compositions at position B in mole fractions $\boldsymbol{x}_{\mathrm{eq,B}}$ and equilibrium temperatures at position B $T_{\mathrm{eq,B}}$.

Experiment	$x_{\mathrm{CH_4,eq,B}}$	$x_{\mathrm{CO,eq,B}}$	$x_{\mathrm{CO_2,eq,B}}$	$x_{\mathrm{H_2,eq,B}}$	$x_{\mathrm{H_2O,eq,B}}$	$x_{\mathrm{N_2,eq,B}}$	$x_{\mathrm{NH_3,eq,B}}$	$x_{\mathrm{H_2S,eq,B}}$	$\dfrac{T_{\mathrm{eq,B}}}{\mathrm{K}}$
V82	0.00000	0.16434	0.12919	0.18002	0.45577	0.07064	0.00004	0.00000	1619
V83	0.00001	0.16937	0.12300	0.19849	0.43272	0.07634	0.00005	0.00000	1569
V84	0.00000	0.15674	0.12992	0.16666	0.46263	0.08401	0.00003	0.00000	1649
V85	0.00003	0.29014	0.11715	0.22766	0.27916	0.08568	0.00006	0.00008	1578

The equilibrium model accordingly predicts the typical low equilibrium

concentrations of CH_4 at high-temperature conditions. Even the equilibrium concentrations of NH_3 are higher than the concentrations of CH_4 for the bioliq EFG experiments V82, V83 and V84 when nitrogen-free ethylene glycol was applied as liquid fuel. Furthermore, the equilibrium model predicts tiny concentrations of higher hydrocarbons, HCN and HCl and zero concentrations of solid carbon. The equilibrium carbon conversion CC_{eq} is thus 100% for each of the four bioliq EFG experiments. Therefore, the equilibrium model provides data for the maximum attainable cold gas efficiency and the maximum attainable synthesis gas yield (see Section 4.2.5).

4.2.4. Comparison of temperatures and gas compositions

The different approximations for the gas temperature at position B $T_{\text{gas,B}}$ are compared for the four bioliq EFG experiments in Fig. 5. The uncertainty bars were obtained from balancing calculations using the minimum and maximum mass flow rates of N_2 as the mass flow rate of N_2 affects the balancing and equilibrium predictions most (see Section 4.3.1). The conclusions are summarised below:

1. The WGS temperatures $T_{\text{WGS,B}}$ of the bioliq EFG experiments V82, V83, V84 and V85 are expected to provide the most accurate approximations of the gas temperatures $T_{\text{gas,B}}$ due to the high cooling rates in the quench.

2. The balanced temperatures $T_{\text{bal,B}}$ are always higher than the WGS temperatures $T_{\text{WGS,B}}$ because peripheral heat losses were not accounted for (see Section 4.3.2).

3. The difference between the balanced temperature $T_{\text{bal,B}}$ and the WGS temperature $T_{\text{WGS,B}}$ is similar for all bioliq EFG experiments. This indicates for the bioliq EFG experiment V85 that the fuel analysis data is sufficiently accurate (see Section 4.3.3).

4. The equilibrium temperatures $T_{\text{eq,B}}$ are significantly lower than the balanced temperatures $T_{\text{bal,B}}$, except for the bioliq EFG experiment V82 with approximately complete carbon conversion (see Section 4.2.1). The biggest difference between equilibrium temperature $T_{\text{eq,B}}$ and balanced

temperature $T_{\mathrm{bal,B}}$ is found for the bioliq EFG experiment V85 with the lowest carbon conversion.

5. The bioliq EFG experiment V84 has higher characteristic temperatures than the bioliq EFG experiments V82 and V83 due to a higher stoichiometric ratio and a lower heat extraction due to higher glass input.

The N_2-free synthesis gas compositions based on measurements, balancing and equilibrium calculations are compared for the bioliq EFG experiment V82 in Fig. 6 and for the bioliq EFG experiment V85 in Fig. 7. The conclusions are summarised below:

1. For the bioliq EFG experiment V82 with high carbon conversion and low methane content and without significant CO_2 loss due to solution and dissociation, the dry gas species concentrations measured at position C are in good agreement with the equilibrium dry gas species concentrations at position B or position C and in excellent agreement with the balanced dry gas species concentrations at position B. The equilibrium model is thus able to provide accurate predictions of the gas species concentrations at positions B and C. Small differences in the gas species concentrations are caused by peripheral heat losses and resulting adjustment of the WGS composition.

2. For the bioliq EFG experiment V85 with the lowest carbon conversion, the equilibrium composition deviates more from the balanced composition than for the other bioliq EFG experiments. The higher CO_2 loss due to solution and dissociation increases the deviations between the dry gas species concentrations at position B and the dry gas species concentrations at position C. This applies especially to CO_2.

4.2.5. Comparison of characteristic parameters

The balanced cold gas efficiencies CGE_{bal} and the balanced yields Y_{bal} are compared with the equilibrium cold gas efficiencies CGE_{eq} and the equilibrium yields Y_{eq} in Table S18 and in Fig. 8. The conclusions are summarised below:

1. The balanced values are always lower than the respective equilibrium values as the balancing model predicts incomplete fuel conversion and the equilibrium model is based on complete fuel conversion. Accordingly, the gap between the balanced values and the equilibrium values is quite small for the bioliq EFG experiment V82 with nearly complete fuel conversion, while larger gaps are found for the bioliq EFG experiments V83, V84 and V85 despite characteristic temperatures above $1500\,\mathrm{K}$ (see [35, 38, 39]) indicating the optimisation potential (e.g. via better atomisation; see [77, 78]).

2. The cold gas efficiency increases with increasing thermal input and decreasing relative total heat extraction of the reactor. Therefore, the cold gas efficiency is highest for the bioliq EFG experiment V85 and is lowest for the bioliq EFG experiment V84.

3. The cold gas efficiency is affected by nitrogen purging streams. For the four bioliq EFG experiments, the cold gas efficiency can be improved by up to two percentage points when avoiding such streams.

4. The balanced cold gas efficiencies CGE_{bal} are in the range of cold gas efficiencies reported for pilot-scale entrained flow gasification experiments with more caloric fuels [18].

5. The equilibrium cold gas efficiency CGE_{eq} is almost linearly related to the stoichiometric ratio λ regardless of the fuel.

The carbon conversions based on the waste water method CC_{ww}, the ash tracer method CC_{at} and both the waste water method and the ash tracer method CC_{ww+at} are given in Table 10.

Table 10: Carbon conversions based on the waste water method CC_{ww}, the ash tracer method CC_{at} and both the waste water method and the ash tracer method CC_{ww+at}.

Experiment	$\dfrac{CC_{ww}}{\%}$	$\dfrac{CC_{at}}{\%}$	$\dfrac{CC_{ww+at}}{\%}$
V82	99.95	> 99.99	> 99.94
V83	99.81	> 99.99	> 99.80
V84	99.85	> 99.98	> 99.82
V85	99.87	99.97	99.84

The carbon conversions derived from the carbon contents of the slag samples CC_{at} and the carbon conversions determined from the TOC contents of the waste water samples CC_{ww} are accordingly above 99.8 % and significantly higher than the balanced carbon conversions CC_{bal} for the bioliq EFG experiments V83, V84 and V85 (see Table 7). However, both the ash tracer method and the waste water method likely overestimate the carbon conversion as neither method accounts for carbon carriers such as higher gaseous hydrocarbons and tars. Therefore, the carbon conversions CC_{at} and CC_{ww} are not recommended to determine carbon conversion. In contrast, good predictions of carbon conversion can be obtained when accounting for lost carbon in elemental balances.

4.3. Sensitivity analyses

The balancing results are strongly coupled with the analysis and measurement data through the solution of the elemental balance equations (see Section 3.4). Therefore, the influences of the analysis and measurement data and the model assumptions regarding both the balancing results and the equilibrium results were investigated with an emphasis on the bioliq EFG experiments V82 and V85.

4.3.1. Feed streams and dry gas species concentrations

The impact of the feed data at position A, the heat extraction and the dry gas species concentrations at position C on the balancing and equilibrium

results was investigated considering the bioliq EFG experiment V82. The uncertainties of the feed data at position A were determined using the minimum and maximum values of the respective quantities (time-averaged every five seconds) during the period of time with stationary conditions, whereas the uncertainty of the heat extraction was derived using Eq. (14) and the uncertainties of the gas species concentrations at position C were defined using the tolerances of the manufacturer. This was reasonable as the tolerances of the measurement devices are mainly lower than the fluctuations of the recorded or balanced data. For selected cases, the deviations from the baseline WGS temperature at position B $\Delta T_{\mathrm{WGS,B}}$, the baseline balanced temperature at position B $\Delta T_{\mathrm{bal,B}}$, the baseline equilibrium temperature at position B $\Delta T_{\mathrm{eq,B}}$, the baseline balanced carbon conversion $\Delta \mathrm{CC}_{\mathrm{bal}}$ and the baseline CO_2 loss $\Delta \mathrm{CO2L}$ are given in Table 11.

Table 11: Impact of the feed data on the balancing and equilibrium results of the bioliq EFG experiment V82: deviations from the baseline WGS temperature at position B $\Delta T_{\mathrm{WGS,B}}$, the baseline balanced temperature at position B $\Delta T_{\mathrm{bal,B}}$, the baseline equilibrium temperature at position B $\Delta T_{\mathrm{eq,B}}$, the baseline balanced carbon conversion $\Delta \mathrm{CC}_{\mathrm{bal}}$ and the baseline CO_2 loss $\Delta \mathrm{CO2L}$.

Experiment	Case	$\dfrac{\Delta T_{\mathrm{WGS,B}}}{\mathrm{K}}$	$\dfrac{\Delta T_{\mathrm{bal,B}}}{\mathrm{K}}$	$\dfrac{\Delta T_{\mathrm{eq,B}}}{\mathrm{K}}$	$\dfrac{\Delta \mathrm{CC}_{\mathrm{bal}}}{\%}$	$\dfrac{\Delta \mathrm{CO2L}}{\%}$
V82	$+0.5\,\% \, \dot{m}_{\mathrm{slurry,A}}$	$+5.3$	-2.6	-6.6	-0.6	-0.2
	$+1.6\,\% \, \dot{m}_{\mathrm{O_2,A}}$	-15.7	$+11.8$	$+35.3$	$+1.2$	$+2.4$
	$+1.5\,\% \, \dot{m}_{\mathrm{steam,A}}$	$+3.9$	-2.8	-2.6	$+0.0$	$+0.0$
	$-12.5\,\% \, \dot{m}_{\mathrm{N_2,A}}$	$+41.2$	$+62.7$	$+8.2$	-7.2	$+11.1$
	$+5.2\,\% \, \dot{Q}_{\mathrm{tot}}$	$-$	-25.6	-24.6	$-$	$-$
	$+1.0\,\% \, x_{\mathrm{CO,meas,dry,C}}$	-10.5	-2.6	$-$	$+0.3$	-0.6
	$+1.0\,\% \, x_{\mathrm{H_2,meas,dry,C}}$	-13.1	-1.8	$-$	$+0.3$	$+0.7$
	$+1.0\,\% \, x_{\mathrm{CO_2,meas,dry,C}}$	$+0.0$	-0.0	$-$	$+0.0$	-1.0
	$+1.0\,\% \, x_{\mathrm{N_2,meas,dry,C}}$	$+3.9$	$+4.4$	$-$	-0.6	$+0.9$

The elemental balances are accordingly very sensitive to the mass flow rate

of N_2, as N_2 was supplied to the reactor for purging at multiple positions using strongly fluctuating flow rates to uphold necessary pressure differences for safe plant operation. Therefore, the supply of N_2 for purging and, consequently, the use of optical measurement systems in pilot-scale experiments should be minimised to obtain superior measurement and balancing data.

4.3.2. Assumptions

The balancing model and the equilibrium model are based on the assumptions that peripheral heat losses can be neglected and that the atomic hydrogen/carbon loss ratio HCR_{loss} is zero. In order to evaluate these model assumptions, balancing and equilibrium calculations were performed using (i) a heat loss of $50\,kW$ and (ii) an atomic hydrogen/carbon loss ratio $HCR_{loss} = 0.8$, which is the hydrogen/carbon ratio of naphthalene (a generic marker for tar [61]). The deviations from the baseline WGS temperature at position B $\Delta T_{WGS,B}$, the baseline balanced temperature at position B $\Delta T_{bal,B}$, the baseline equilibrium temperature at position B $\Delta T_{eq,B}$, the baseline balanced carbon conversion ΔCC_{bal} and the baseline CO_2 loss $\Delta CO2L$ are listed for the bioliq EFG experiments V82 and V85 in Table 12.

Table 12: Impact of the model assumptions on the balancing and equilibrium results of the bioliq EFG experiments V82 and V85: deviations from the baseline WGS temperature at position B $\Delta T_{WGS,B}$, the baseline balanced temperature at position B $\Delta T_{bal,B}$, the baseline equilibrium temperature at position B $\Delta T_{eq,B}$, the baseline balanced carbon conversion ΔCC_{bal} and the baseline CO_2 loss $\Delta CO2L$.

Experiment	Case	$\dfrac{\Delta T_{WGS,B}}{K}$	$\dfrac{\Delta T_{bal,B}}{K}$	$\dfrac{\Delta T_{eq,B}}{K}$	$\dfrac{\Delta CC_{bal}}{\%}$	$\dfrac{\Delta CO2L}{\%}$
V82	$\dot{Q}_{loss} = 50\,kW$	–	−44.7	−42.9	–	–
	$HCR_{loss} = 0.8$	−1.3	+3.8	–	+0.1	+0.2
V85	$\dot{Q}_{loss} = 50\,kW$	–	−48.7	+46.7	–	–
	$HCR_{loss} = 0.8$	−45.9	+60.0	–	+1.1	+3.3

For the bioliq EFG experiments V82 and V85, the balanced

temperature $T_{\mathrm{bal,B}}$ is approximately $50\,\mathrm{K}$ lower in the presence of a heat loss of about $50\,\mathrm{kW}$, which improves the agreement with the WGS temperature $T_{\mathrm{WGS,B}}$. Furthermore, changes in the atomic hydrogen/carbon loss ratio $\mathrm{HCR_{loss}}$, which typically increases for experiments with decreasing gas temperatures and carbon conversions, do not affect the predictions for the bioliq EFG experiment V82 due to nearly complete carbon conversion. In contrast, for the bioliq EFG experiment V85, a higher atomic hydrogen/carbon loss ratio $\mathrm{HCR_{loss}}$ significantly changes the predictions.

4.3.3. Chemical beech wood pyrolysis oil properties

The impact of the chemical beech wood pyrolysis oil properties on both the balancing results and the equilibrium results of the bioliq EFG experiment V85 was investigated using the analysis results of the internal and external laboratories (see Section 3.1.2). Equilibrium temperatures $T_{\mathrm{eq,B}}$, balanced temperatures $T_{\mathrm{bal,B}}$ and WGS temperatures $T_{\mathrm{WGS,B}}$, each at position B, are compared in Fig. 9 and Table S19. The equilibrium temperature $T_{\mathrm{eq,B}}$ scatters accordingly more than $380\,\mathrm{K}$ while the difference between the balanced temperatures $T_{\mathrm{bal,B}}$ and the WGS temperatures $T_{\mathrm{WGS,B}}$ is between $65\,\mathrm{K}$ and $615\,\mathrm{K}$. In contrast, the difference is typically less than $55\,\mathrm{K}$ for the bioliq EFG experiments with well-defined surrogate fuels (only reflecting peripheral heat losses). This demonstrates discrepancies in measured compositions and heating values and a high model sensitivity of both the balancing model and the equilibrium model regarding the analysis results. In this study, the analysis results of laboratory II provided the best agreement of the balanced temperature $T_{\mathrm{bal,B}}$ with the WGS temperature $T_{\mathrm{WGS,B}}$.

Furthermore, the balanced temperature $T_{\mathrm{bal,B}}$, in both the presence and the absence of peripheral heat losses, and the WGS temperature $T_{\mathrm{WGS,B}}$ are plotted over the Boie ratio in Fig. 10. The plot indicates that (i) the balanced temperatures $T_{\mathrm{bal,B}}$ and the WGS temperatures $T_{\mathrm{WGS,B}}$ are strongly coupled with the Boie ratio, (ii) the difference between the balanced temperature $T_{\mathrm{bal,B}}$ and the WGS temperature $T_{\mathrm{WGS,B}}$ should be small when using accurate fuel

analysis results and appropriate balancing assumptions and (iii) the heating value calculated using the Boie correlation [75] should be close to the measured heating value. As the identification of accurate analysis results is crucial for the evaluation, design or scale-up of entrained flow gasification processes and is certainly not trivial [60], future studies should prove these theses using gas temperature measurements inside the inner reactor chamber.

4.3.4. Chemical natural gas properties

The impact of the chemical natural gas properties on the equilibrium results was analysed considering the bioliq EFG experiment V82 as CFD models typically require a simplified natural gas composition adjusted to the reaction mechanism. A strongly simplified composition was determined from the detailed composition neglecting higher hydrocarbons and is given in Table 2. The equilibrium compositions at position B in mole fractions $\boldsymbol{x}_{\mathrm{eq,B}}$ and the equilibrium temperatures $T_{\mathrm{eq,B}}$ based on both the detailed composition and the simplified composition are compared in Table 13. Similar equilibrium results were accordingly obtained using both the detailed and the simplified composition. Thus, simplified natural gas compositions are doable for the CFD simulations of the bioliq EFG experiments as even strong simplifications of the natural gas composition do not significantly affect the results for the gas condition at the outlet of the inner reactor chamber.

Table 13: Impact of the composition of natural gas on the equilibrium results of the bioliq EFG experiment V82: equilibrium compositions at position B in mole fractions $\boldsymbol{x}_{\mathrm{eq,B}}$ and equilibrium temperatures $T_{\mathrm{eq,B}}$.

Experiment	Case	$x_{\mathrm{CO,eq,B}}$	$x_{\mathrm{CO_2,eq,B}}$	$x_{\mathrm{H_2,eq,B}}$	$x_{\mathrm{H_2O,eq,B}}$	$x_{\mathrm{N_2,eq,B}}$	$\dfrac{T_{\mathrm{eq,B}}}{\mathrm{K}}$
V82	Detailed composition	0.1643	0.1292	0.1800	0.4558	0.0706	1619
	Simplified composition	0.1641	0.1288	0.1808	0.4556	0.0706	1616

5. Conclusions

Balancing and equilibrium models were developed for the optimisation, design and scale-up of high-pressure entrained flow gasification processes with biogenic and anthropogenic fuels and were applied to four bioliq EFG experiments. These experiments were carried out using mixtures of ethylene glycol or beech wood pyrolysis oil with glass beads after recoating the refractory of the cooling screen to ensure well-defined heat transfer conditions. The conclusions based on the evaluation of measurement, balancing and equilibrium data are summarised below:

1. The bioliq EFG plant can be operated using beech wood pyrolysis oil and glass beads for 100 h in a stable manner without slag blocking and with high carbon conversion.

2. The bioliq EFG plant with its measurement capabilities can be used to generate excellent process data for various feedstocks and for performance analysis.

3. The balancing model provides consistent and accurate predictions for the composition and the temperature of the synthesis gas before entering the water quench. The predictions are accurate if (i) all inlet flows are precisely recorded, (ii) the solution of CO_2 in the quench water is accounted for, (iii) undetected intermediates are described as lost carbon and lost atomic hydrogen, (iv) further chemical reactions in the quench water are avoided by the operating conditions and (v) the chemical fuel data is selected using the ratio of the heating value calculated using the Boie correlation [75] to the measured heating value.

4. The equilibrium model is able to track the generated process data and is suitable for scale-up calculations.

5. The water-gas shift temperature, the balanced temperature and the equilibrium temperature enable the evaluation of the process temperature, the heat loss and the fuel analysis data.

6. The balanced carbon conversion should be preferred over the carbon conversion based on the ash tracer method and the carbon conversion based on the waste water method.

7. The local effects of the physical and thermo-chemical sub-processes in the gasifier are decisive for conversion and process efficiency. This requires detailed investigation of atomisation, fuel and flame characterisation, slagging and heat transfer for process optimisation using both experiments and numerical simulations.

Future studies should perform measurements of gas species concentrations and gas temperatures in the inner reactor chamber to validate the condition of the synthesis gas before it enters the water quench. Furthermore, future studies should improve upon the analyses of dissolved and dissociated gases as well as of intermediates and by-products to enhance the element balances. Future studies should also investigate the impact of the quench operating conditions and the quench water composition on the synthesis gas composition. The high solubility of CO_2 might be used to capture and re-use CO_2 and to improve the process efficiency. Finally, future experiments should account for broad variations of operating or process parameters (e.g. fuel quality, steam quantity, temperature and spray quality). Firstly, various biogenic and anthropogenic feedstocks should be applied to generate fuel-specific process databases for evaluation, design and scale-up. Secondly, the operating conditions should be varied to determine the optimum and fuel-specific process conditions and the optimum temperature-dependent parameters for scale-up. Thirdly, the influences of operating limits and process parameters should be investigated for various technical slags.

Figures

Figure 1: Process flow-sheet of the high-pressure gasification of the bioliq pilot plant including the bioliq EFG, the system boundaries of the overall system (depicted with a red border) and the inner reactor chamber (depicted with a yellow border) and characteristic positions A, B, C, D, E, F and G [4, 64].
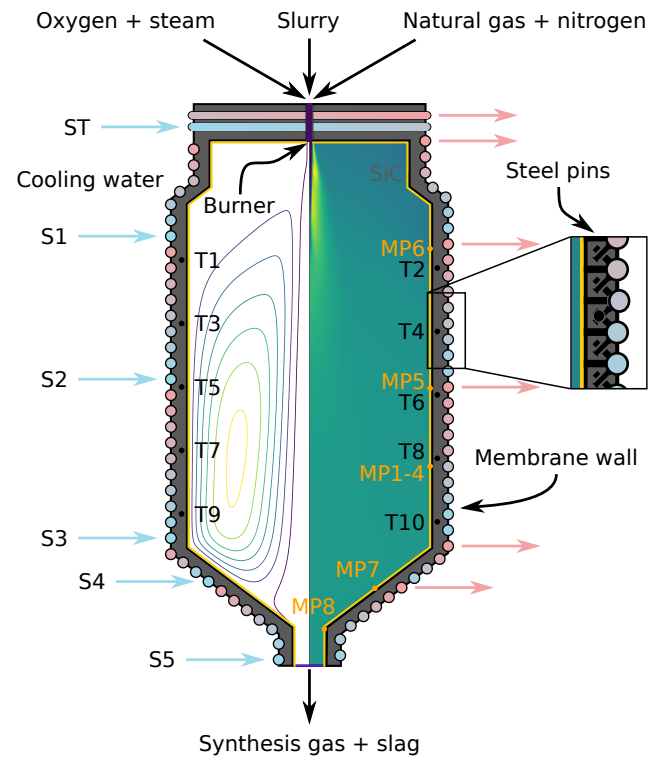
Figure 2: Schematic cross section of the bioliq EFG reactor with the refractory thermocouples placed at positions T1, ..., T10 and the cooling circuits and segments S1, ..., S5 and ST.
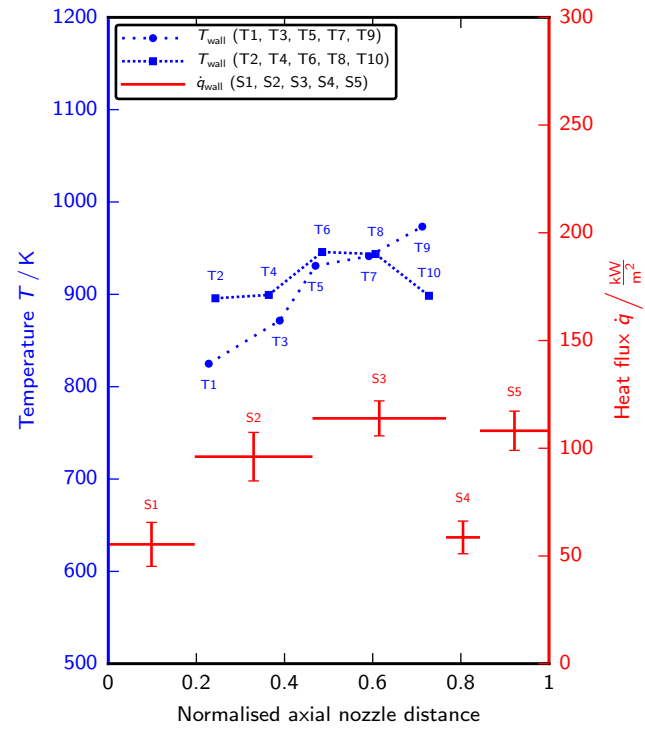
Figure 3: Refractory temperatures and heat fluxes: comparison for the bioliq EFG experiment V85.
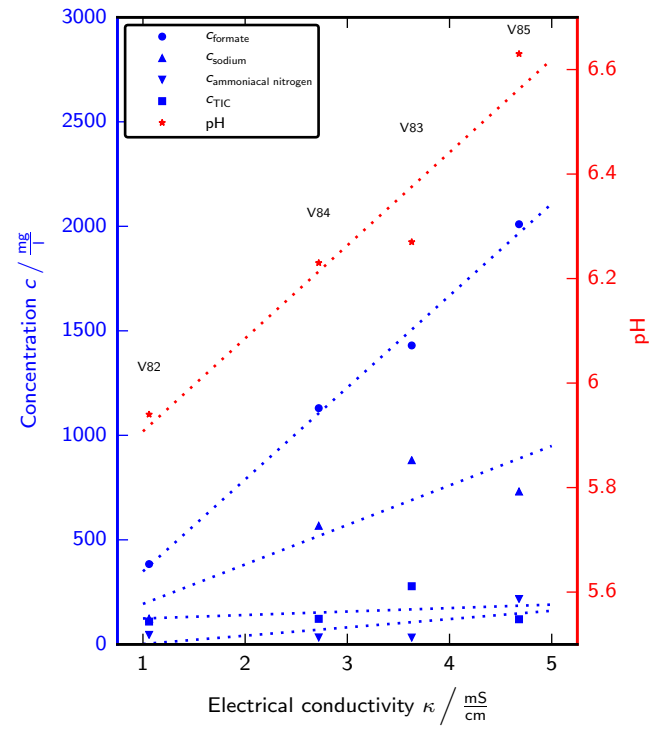
Figure 4: Concentrations of formate, sodium, ammoniacal nitrogen and TIC as well as pH: comparison for the waste water samples from the bioliq EFG experiments V82, V83, V84 and V85.
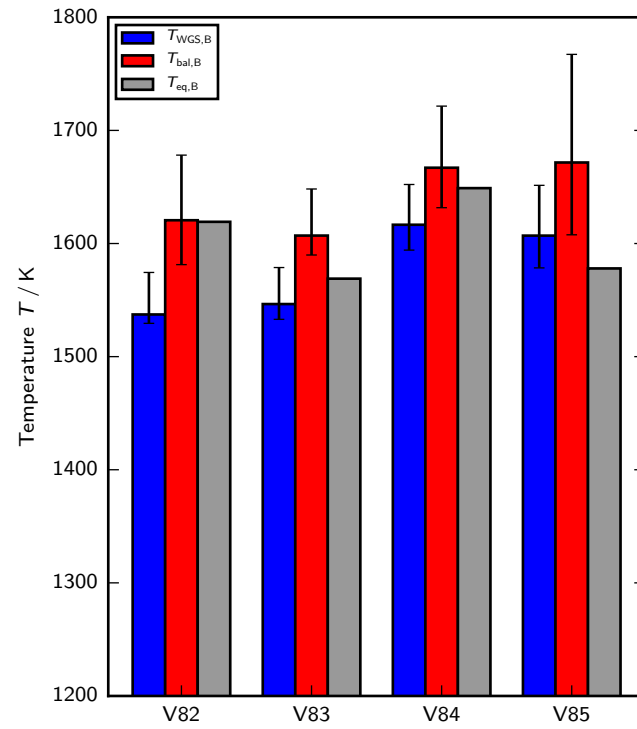
Figure 5: WGS temperatures at position B $T_{\mathrm{WGS,B}}$, balanced temperatures at position B $T_{\mathrm{bal,B}}$ and equilibrium temperatures at position B $T_{\mathrm{eq,B}}$.
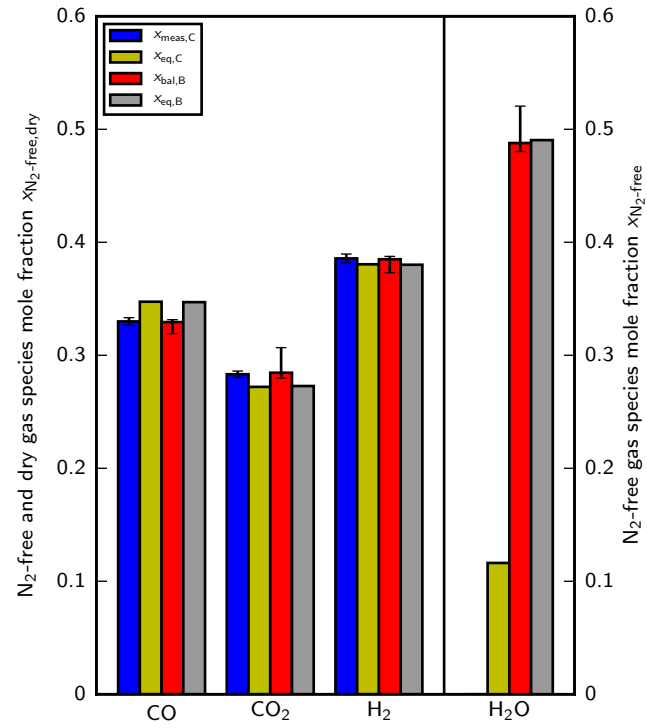
Figure 6: Balanced N_2-free gas species mole fractions at position B $\boldsymbol{x}_{\mathrm{bal},N_2\text{-free},B}$, equilibrium N_2-free gas species mole fractions at position B $\boldsymbol{x}_{\mathrm{eq},N_2\text{-free},B}$, equilibrium-derived N_2-free gas species mole fractions at position C $\boldsymbol{x}_{\mathrm{eq},N_2\text{-free},C}$ and measured N_2-free gas species mole fractions at position C $\boldsymbol{x}_{\mathrm{meas},N_2\text{-free},C}$: comparison for the bioliq EFG experiment V82.
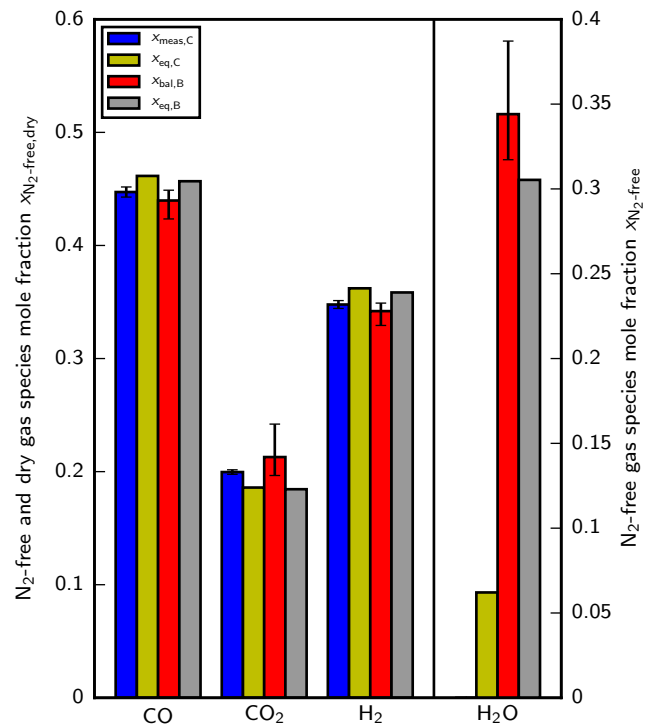
Figure 7: Balanced N_2-free gas species mole fractions at position B $\boldsymbol{x}_{\text{bal},N_2\text{-free},B}$, equilibrium N_2-free gas species mole fractions at position B $\boldsymbol{x}_{\text{eq},N_2\text{-free},B}$, equilibrium-derived N_2-free gas species mole fractions at position C $\boldsymbol{x}_{\text{eq},N_2\text{-free},C}$ and measured N_2-free gas species mole fractions at position C $\boldsymbol{x}_{\text{meas},N_2\text{-free},C}$: comparison for the bioliq EFG experiment V85.
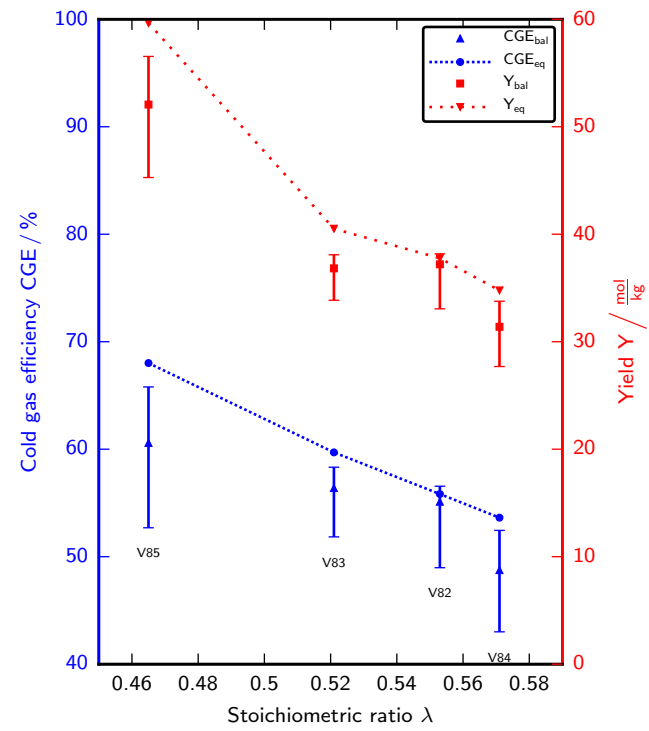
Figure 8: Balanced cold gas efficiencies CGE_{bal}, equilibrium cold gas efficiencies CGE_{eq}, balanced yields Y_{bal} and equilibrium yields Y_{eq}.
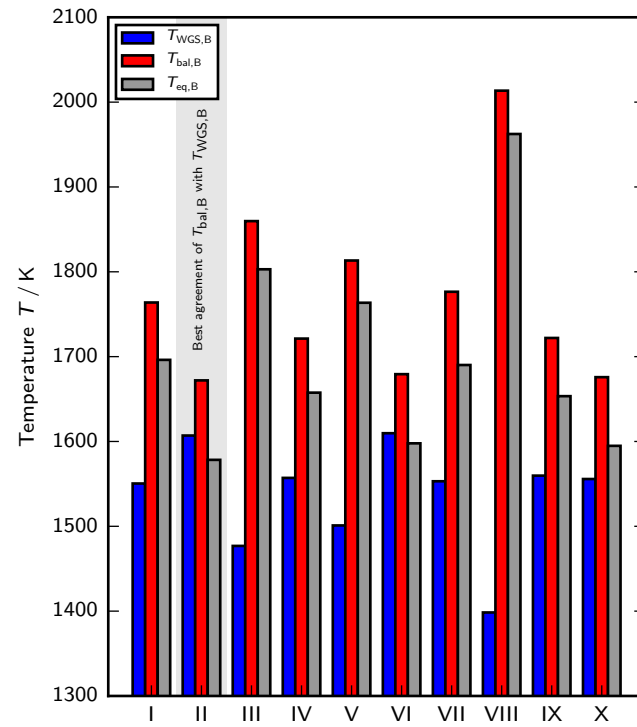
Figure 9: WGS temperatures at position B $T_{\mathrm{WGS,B}}$, balanced temperatures at position B $T_{\mathrm{bal,B}}$ and equilibrium temperatures at position B $T_{\mathrm{eq,B}}$: comparison for the bioliq EFG experiment V85 considering different analysis results.
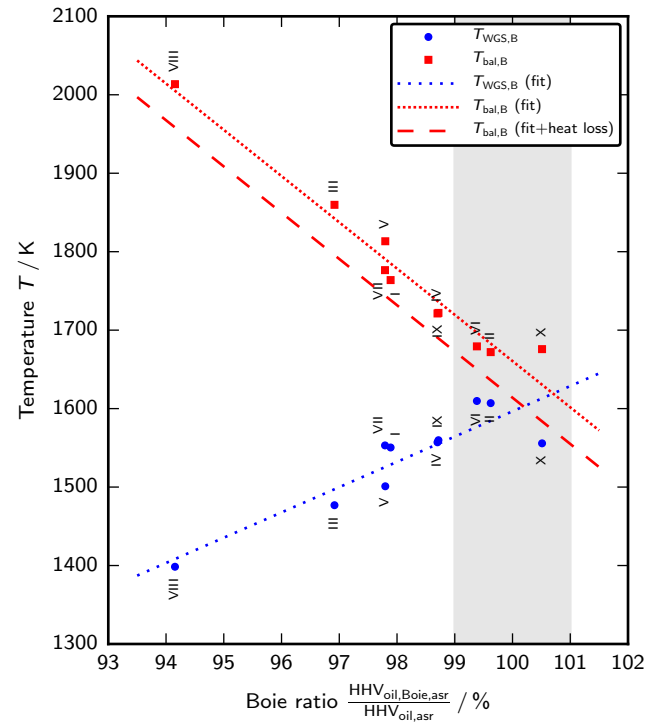
Figure 10: WGS temperatures at position B $T_{WGS,B}$ and balanced temperatures at position B $T_{bal,B}$ plotted over Boie ratio $HHV_{Boie,oil,asr}/HHV_{oil,asr}$: comparison for the bioliq EFG experiment V85 considering different analysis results.

References

[1] N. Dahmen, J. Abeln, M. Eberhard, T. Kolb, H. Leibold, J. Sauer, D. Stapf, B. Zimmerlin, The bioliq process for producing synthetic transportation fuels, WIREs Energy and Environment 6 (3). `doi:10.1002/wene.236`.
URL `https://doi.org/10.1002/wene.236`

[2] M. Dammann, M. Mancini, R. Weber, T. Kolb, Entrained flow gasification: mathematical modelling based on RANS for design and scale-up, in: Proceedings of the 30th Deutscher Flammentag: für nachhaltige Verbrennung, 28-29 September 2021, Hannover-Garbsen, Germany, Deutsche Vereinigung für Verbrennungsforschung and The Combustion Institute Deutsche Sektion, Hannover-Garbsen, Germany, 2021. `doi:10.5445/IR/1000140359`.
URL `https://doi.org/10.5445/IR/1000140359`

[3] Karlsruhe Institute of Technology, bioliq (2021).
URL `https://www.bioliq.de/`

[4] M. Eberhard, U. Santo, B. Michelfelder, A. Günther, P. Weigand, J. Matthes, P. Waibel, V. Hagenmeyer, T. Kolb, The bioliq® Entrained Flow Gasifier: a model for the German Energiewende, ChemBioEng Reviews 7 (4) (2020) 106–118. `doi:10.1002/cben.202000006`.
URL `https://doi.org/10.1002/cben.202000006`

[5] S. Seebold, M. Eberhard, G. Wu, E. Yazhenskikh, D. Sergeev, T. Kolb, M. Müller, Thermophysical and chemical properties of bioliq slags, Fuel 197 (2017) 596–604. `doi:10.1016/j.fuel.2017.02.027`.
URL `https://doi.org/10.1016/j.fuel.2017.02.027`

[6] C. Chen, M. Horio, T. Kojima, Numerical simulation of entrained flow coal gasifiers. Part I: modeling of coal gasification in an entrained flow gasifier, Chemical Engineering Science 55 (18) (2000) 3861–3874. `doi:10.1016/s0009-2509(00)00030-0`.
URL `https://doi.org/10.1016/S0009-2509(00)00030-0`

[7] M. Marklund, Pressurized entrained-flow high temperature black liquor gasification: CFD based reactor scale-up method and spray burner characterization, Ph.D. Thesis, Department of Engineering Sciences and Mathematics, Luleå University of Technology, Luleå, Sweden (2006).
URL https://nbn-resolving.org/urn:nbn:se:ltu:diva-26275

[8] H. Wiinikka, P. Carlsson, F. Granberg, J. Löfström, M. Marklund, R. Tegman, M. Lindblom, R. Gebart, Design and methodology of a high temperature gas sampling system for pressurized black liquor gasification, Fuel 89 (9) (2010) 2583–2591. doi:10.1016/j.fuel.2010.02.021.
URL https://doi.org/10.1016/j.fuel.2010.02.021

[9] M. Vascellari, D. G. Roberts, S. S. Hla, D. J. Harris, C. Hasse, From laboratory-scale experiments to industrial-scale CFD simulations of entrained flow coal gasification, Fuel 152 (2015) 58–73. doi:10.1016/j.fuel.2015.01.038.
URL https://doi.org/10.1016/j.fuel.2015.01.038

[10] P. Brüggemann, Formation and evolution of by-products and trace substances in the high pressure partial oxidation of gaseous and liquid hydrocarbons, Ph.D. Thesis, Fakultät für Maschinenbau, Technische Universität Bergakademie Freiberg, Freiberg, Germany (Sep. 2010).

[11] P. Carlsson, H. Wiinikka, M. Marklund, C. Grönberg, E. Pettersson, M. Lidman, R. Gebart, Experimental investigation of an industrial scale black liquor gasifier. 1. The effect of reactor operation parameters on product gas composition, Fuel 89 (12) (2010) 4025–4034. doi:10.1016/j.fuel.2010.05.003.
URL https://doi.org/10.1016/j.fuel.2010.05.003

[12] K. Covella, S. M. Cavagnol, M. Müller-Hagedorn, B. Zimmerlin, T. Kolb, Data validation and reconciliation of entrained-flow gasification with Aspen plus, in: Proceedings of the 9th International Freiberg Conference on IGCC

& XtL Technologies, 3-8 June 2018, Berlin, Germany, Berlin, Germany, 2018.

[13] A. M. Robin, Hydrogen production from coal liquefaction residues, Tech. Rep. EPRI AF-233, EPRI, Montebello, CA, USA (Dec. 1976). `doi:10.2172/7117259`.
URL `https://doi.org/10.2172/7117259`

[14] A. Richter, P. Seifert, F. Compart, P. Tischer, B. Meyer, A large-scale benchmark for the CFD modeling of non-catalytic reforming of natural gas based on the Freiberg test plant HP POX, Fuel 152 (2015) 110–121. `doi:10.1016/j.fuel.2014.12.004`.
URL `https://doi.org/10.1016/j.fuel.2014.12.004`

[15] Z. Sun, Z. Dai, Z. Zhou, Q. Guo, G. Yu, Numerical simulation of industrial opposed multiburner coal-water slurry entrained flow gasifier, Industrial & Engineering Chemistry Research 51 (6) (2012) 2560–2569. `doi:10.1021/ie201542q`.
URL `https://doi.org/10.1021/ie201542q`

[16] F. Weiland, Pressurized entrained flow gasification of pulverized biomass: experimental characterization of process performance, Ph.D. Thesis, Department of Engineering Sciences and Mathematics, Luleå University of Technology, Luleå, Sweden (2015).
URL `https://nbn-resolving.org/urn:nbn:se:ltu:diva-18610`

[17] H. Wiinikka, P. Carlsson, M. Marklund, C. Grönberg, E. Pettersson, M. Lidman, R. Gebart, Experimental investigation of an industrial scale black liquor gasifier. Part 2: influence of quench operation on product gas composition, Fuel 93 (2012) 117–129. `doi:10.1016/j.fuel.2011.06.066`.
URL `https://doi.org/10.1016/j.fuel.2011.06.066`

[18] D. G. Roberts, A. Y. Ilyushechkin, D. J. Harris, Linking laboratory data with pilot scale entrained flow coal gasification performance. Part

1: laboratory characterisation, Fuel Processing Technology 94 (1) (2012) 86–93. doi:10.1016/j.fuproc.2011.10.013.
URL https://doi.org/10.1016/j.fuproc.2011.10.013

[19] D. G. Roberts, D. J. Harris, A. Tremel, A. Y. Ilyushechkin, Linking laboratory data with pilot scale entrained flow coal gasification performance. Part 2: pilot scale testing, Fuel Processing Technology 94 (1) (2012) 26–33. doi:10.1016/j.fuproc.2011.10.011.
URL https://doi.org/10.1016/j.fuproc.2011.10.011

[20] Y. Jafri, E. Furusjö, K. Kirtania, R. Gebart, Performance of a pilot-scale entrained-flow black liquor gasifier, Energy & Fuels 30 (4) (2016) 3175–3185. doi:10.1021/acs.energyfuels.6b00349.
URL ttps://doi.org/10.1021/acs.energyfuels.6b00349

[21] Y. Jafri, E. Furusjö, K. Kirtania, R. Gebart, F. Granberg, A study of black liquor and pyrolysis oil co-gasification in pilot scale, Biomass Conversion and Biorefinery 8 (1) (2018) 113–124. doi:10.1007/s13399-016-0235-5.
URL https://doi.org/10.1007/s13399-016-0235-5

[22] Cool water coal gasification program: final report, Tech. Rep. EPRI GS-6806, Daggett, CA, USA (Dec. 1990).
URL https://www.epri.com/research/products/GS-6806

[23] M. J. Hornick, J. E. McDaniel, Tampa Electric Polk power station integrated gasification combined cycle project: final technical report, Tech. rep., Tampa Electric, Morgantown, WV, USA (Aug. 1996).

[24] H. Liu, T. Kojima, C. Chen, Interaction between a turbulent flow and reaction under various conditions in oxygen blown HYCOL gasifiers, Developments in Chemical Engineering and Mineral Processing 11 (5-6) (2003) 557–577. doi:10.1002/apj.5500110613.
URL https://doi.org/10.1002/apj.5500110613

[25] H. Liu, T. Kojima, Theoretical study of coal gasification in a 50 ton/day HYCOL entrained flow gasifier. II. Effects of operating conditions and comparison with pilot-scale experiments, Energy & Fuels 18 (4) (2004) 913–917. `doi:10.1021/ef030163j`.
URL `https://doi.org/10.1021/ef030163j`

[26] National Energy Technology Laboratory, Wabash River coal gasification repowering project: a DOE assessment, Tech. rep., U.S. Department of Energy, National Energy Technology Laboratory, Morgantown, WV, USA (Jan. 2002). `doi:10.2172/790376`.
URL `https://doi.org/10.2172/790376`

[27] The Tampa Electric integrated gasification combined cycle project: demonstration of an advanced 250 Megawatt integrated gasification combined-cycle power plant, Tech. rep., Tampa Electric, Morgantown, WV, USA (Aug. 1996).

[28] Y. Wu, J. Zhang, P. J. Smith, H. Zhang, C. Reid, J. Lv, G. Yue, Three-dimensional simulation for an entrained flow coal slurry gasifier, Energy & Fuels 24 (2) (2010) 1156–1163. `doi:10.1021/ef901085b`.
URL `https://doi.org/10.1021/ef901085b`

[29] J. Xu, Q. Liang, Z. Dai, H. Liu, Comprehensive model with time limited wall reaction for entrained flow gasifier, Fuel 184 (2016) 118–127. `doi: 10.1016/j.fuel.2016.06.122`.
URL `https://doi.org/10.1016/j.fuel.2016.06.122`

[30] J. Xu, H. Zhao, Z. Dai, H. Liu, F. Wang, Numerical simulation of opposed multi-burner gasifier under different coal loading ratio, Fuel 174 (2016) 97–106. `doi:10.1016/j.fuel.2016.01.079`.
URL `https://doi.org/10.1016/j.fuel.2016.01.079`

[31] J. Xu, Z. Dai, H. Liu, L. Guo, F. Sun, Modeling of multiphase reaction and slag flow in single-burner coal water slurry gasifier, Chemical Engineering

Science 162 (2017) 41–52. `doi:10.1016/j.ces.2016.12.029`.
URL `https://doi.org/10.1016/j.ces.2016.12.029`

[32] A. C. Beath, Mathematical modelling of entrained flow coal gasification, Ph.D. Thesis, Department of Chemical Engineering, University of Newcastle, Newcastle, NSW, Australia (Mar. 1996).

[33] P. Carlsson, M. Marklund, E. Furusjö, H. Wiinikka, R. Gebart, Black liquor gasification. CFD model predictions compared with measurements, in: Conference Proceedings of the 2010 International Chemical Recovery Conference, 29 March-1 April 2010, Williamsburg, VA, USA, Vol. 2, TAPPI, Williamsburg, VA, USA, 2010, pp. 160–171.
URL `https://imisrise.tappi.org/TAPPI/Products/10/ICR/10ICRC53.aspx`

[34] Z. Dai, X. Gong, X. Guo, H. Liu, F. Wang, Z. Yu, Pilot-trial and modeling of a new type of pressurized entrained-flow pulverized coal gasification technology, Fuel 87 (10-11) (2008) 2304–2313. `doi:10.1016/j.fuel.2007.12.005`.
URL `https://doi.org/10.1016/j.fuel.2007.12.005`

[35] P. Feng, W. Lin, P. A. Jensen, W. Song, L. Hao, K. Raffelt, K. Dam-Johansen, Entrained flow gasification of coal/bio-oil slurries, Energy 111 (2016) 793–802. `doi:10.1016/j.energy.2016.05.115`.
URL `http://doi.org/10.1016/j.energy.2016.05.115`

[36] H. Ghassemi, R. Shahsavan-Markadeh, Effects of various operational parameters on biomass gasification process: a modified equilibrium model, Energy Conversion and Management 79 (2014) 18–24. `doi:10.1016/j.enconman.2013.12.007`.
URL `http://doi.org/10.1016/j.enconman.2013.12.007`

[37] X. Kong, W. Zhong, W. Du, F. Qian, Three stage equilibrium model for coal gasification in entrained flow gasifiers based on Aspen Plus, Chinese

Journal of Chemical Engineering 21 (1) (2013) 79–84. `doi:10.1016/s1004-9541(13)60444-9`.
URL `https://doi.org/10.1016/s1004-9541(13)60444-9`

[38] L. Mazzoni, M. Almazrouei, C. Ghenai, I. Janajreh, A comparison of energy recovery from MSW through plasma gasification and entrained flow gasification, Energy Procedia 142 (2017) 3480–3485. `doi:10.1016/j.egypro.2017.12.233`.
URL `https://doi.org/10.1016/j.egypro.2017.12.233`

[39] F. Trippe, M. Fröhling, F. Schultmann, R. Stahl, E. Henrich, Techno-economic assessment of gasification as a process step within biomass-to-liquid (BtL) fuel and chemicals production, Fuel Processing Technology 92 (11) (2011) 2169–2184. `doi:10.1016/j.fuproc.2011.06.026`.
URL `https://doi.org/10.1016/j.fuproc.2011.06.026`

[40] R. Govind, J. Shah, Modeling and simulation of an entrained flow coal gasifier, AIChE Journal 30 (1) (1984) 79–92. `doi:10.1002/aic.690300113`.
URL `https://doi.org/10.1002/aic.690300113`

[41] J. S. Kasule, R. Turton, D. Bhattacharyya, S. E. Zitney, Mathematical modeling of a single-stage, downward-firing, entrained-flow gasifier, Industrial & Engineering Chemistry Research 51 (18) (2012) 6429–6440. `doi:10.1021/ie202121h`.
URL `https://doi.org/10.1021/ie202121h`

[42] X. Kong, W. Zhong, W. Du, F. Qian, Compartment modeling of coal gasification in an entrained flow gasifier: a study on the influence of operating conditions, Energy Conversion and Management 82 (2014) 202–211. `doi:10.1016/j.enconman.2014.01.055`.
URL `http://doi.org/10.1016/j.enconman.2014.01.055`

[43] G.-S. Liu, H. R. Rezaei, J. A. Lucas, D. J. Harris, T. F. Wall, Modelling of a pressurised entrained flow coal gasifier: the effect of reaction kinetics

and char structure, Fuel 79 (14) (2000) 1767–1779. `doi:10.1016/s0016-2361(00)00037-5`.
URL `https://doi.org/10.1016/S0016-2361(00)00037-5`

[44] T. D. Nguyen, Y.-I. Lim, B.-H. Song, S.-M. Kim, Y.-J. Joo, D.-H. Ahn, Two-stage equilibrium model applicable to the wide range of operating conditions in entrained-flow coal gasifiers, Fuel 89 (12) (2010) 3901–3910. `doi:10.1016/j.fuel.2010.06.044`.
URL `https://doi.org/10.1016/j.fuel.2010.06.044`

[45] P. Schoen, Dynamic modeling and control of integrated coal gasification combined cycle units, Ph.D. Thesis, Delft University of Technology, Delft, The Netherlands (Sep. 1993).
URL `http://resolver.tudelft.nl/uuid:59ae88a4-b5cf-4c71-83e7-c8df8873b6b1`

[46] C. Y. Wen, T. Z. Chaung, Entrainment coal gasification modeling, Industrial & Engineering Chemistry Process Design and Development 18 (4) (1979) 684–695. `doi:10.1021/i260072a020`.
URL `https://doi.org/10.1021/i260072a020`

[47] R. F. D. Monaghan, M. Kumar, S. L. Singer, C. Zhang, A. F. Ghoniem, Reduced order modeling of entrained flow solid fuel gasification, in: Proceedings of the ASME 2009 International Mechanical Engineering Congress & Exposition. Volume 3: Combustion Science and Engineering, 13-19 November 2009, Lake Buena Vista, FL, USA, no. IMECE2009-12985, ASME Digital Collection, Lake Buena Vista, FL, USA, 2009. `doi:10.1115/imece2009-12985`.
URL `https://doi.org/10.1115/IMECE2009-12985`

[48] R. F. D. Monaghan, Dynamic reduced order modeling of entrained flow gasifiers, Ph.D. Thesis, Department of Mechanical Engineering, Massachusetts Institute of Technology, Cambridge, MA, USA (Feb. 2010).
URL `http://hdl.handle.net/1721.1/58191`

[49] R. F. D. Monaghan, A. F. Ghoniem, A dynamic reduced order model for simulating entrained flow gasifiers, Fuel 91 (1) (2012) 61–80. `doi:10.1016/j.fuel.2011.07.015`.
URL `https://doi.org/10.1016/j.fuel.2011.07.015`

[50] R. F. D. Monaghan, A. F. Ghoniem, A dynamic reduced order model for simulating entrained flow gasifiers. Part II: model validation and sensitivity analysis, Fuel 94 (2012) 280–297. `doi:10.1016/j.fuel.2011.08.046`.
URL `https://doi.org/10.1016/j.fuel.2011.08.046`

[51] Y. Lang, S. E. Zitney, L. T. Biegler, Optimization of IGCC processes with reduced order CFD models, Computers & Chemical Engineering 35 (9) (2011) 1705–1717. `doi:10.1016/j.compchemeng.2011.01.018`.
URL `https://doi.org/10.1016/j.compchemeng.2011.01.018`

[52] M. Gazzani, G. Manzolini, E. Macchi, A. F. Ghoniem, Reduced order modeling of the Shell-Prenflo entrained flow gasifier, Fuel 104 (2013) 822–837. `doi:10.1016/j.fuel.2012.06.117`.
URL `https://doi.org/10.1016/j.fuel.2012.06.117`

[53] H. Zhou, T. Xie, F. You, On-line simulation and optimization of a commercial-scale Shell entrained-flow gasifier using a novel dynamic reduced order model, Energy 149 (2018) 516–534. `doi:10.1016/j.energy.2018.02.031`.
URL `https://doi.org/10.1016/j.energy.2018.02.031`

[54] J. Kittel, F. Hannemann, F. Mehlhose, S. Heil, B. Meyer, Dynamic modelling of the heat transfer into the cooling screen of the SFGT-gasifier, in: Proceedings of the 7th International Modelica Conference, 20-22 September 2009, Como, Italy, Linköping University Electronic Press, Como, Italy, 2009, pp. 326–334. `doi:10.3384/ecp09430011`.
URL `https://doi.org/10.3384/ecp09430011`

[55] A. Bader, M. Hartwich, A. Richter, B. Meyer, Numerical and experimental study of heavy oil gasification in an entrained-flow reactor and the impact

of the burner concept, Fuel Processing Technology 169 (2018) 58–70. `doi:10.1016/j.fuproc.2017.09.003`.
URL `https://doi.org/10.1016/j.fuproc.2017.09.003`

[56] M. Dammann, Numerical modelling and simulation of atmospheric entrained flow gasification of surrogate fuels, Ph.D. Thesis, Fakultät für Chemieingenieurwesen und Verfahrenstechnik, Karlsruher Institut für Technologie, Karlsruhe, Germany (2024).

[57] M. Mancini, M. Alberti, M. Dammann, U. Santo, G. Eckel, T. Kolb, R. Weber, Entrained flow gasification. Part 2: mathematical modeling of the gasifier using RANS method, Fuel 225 (2018) 596–611. `doi:10.1016/j.fuel.2018.03.100`.
URL `https://doi.org/10.1016/j.fuel.2018.03.100`

[58] S. Halama, H. Spliethoff, Reaction kinetics of pressurized entrained flow coal gasification: computational fluid dynamics simulation of a 5 MW Siemens test gasifier, Journal of Energy Resources Technology 138 (4). `doi:10.1115/1.4032620`.
URL `https://doi.org/10.1115/1.4032620`

[59] C. Ehnes, Heterogen katalysierte Hydrierung von Kohlendioxid zu Ameisensäure, Ph.D. Thesis, Fachbereich Chemie, Technische Universität Darmstadt, Darmstadt, Germany (Jul. 2016).
URL `https://tuprints.ulb.tu-darmstadt.de/5634`

[60] C. Higman, M. van der Burgt, Gasification, 2nd Edition, Gulf Professional Publishing, Burlington, MA, USA, 2008. `doi:10.1016/b978-0-7506-8528-3.x0001-6`.
URL `https://doi.org/10.1016/b978-0-7506-8528-3.x0001-6`

[61] S. Fleck, U. Santo, C. Hotz, T. Jakobs, G. Eckel, M. Mancini, R. Weber, T. Kolb, Entrained flow gasification. Part 1: gasification of glycol in an atmospheric-pressure experimental rig, Fuel 217 (2018) 306–319. `doi:10.`

1016/j.fuel.2017.12.077.

URL https://doi.org/10.1016/j.fuel.2017.12.077

[62] Aspen Properties. Release V12 (2022).
URL https://www.aspentech.com/products/aspen-properties.aspx

[63] T. J. Edwards, G. Maurer, J. Newman, J. M. Prausnitz, Vapor-liquid equilibria in multicomponent aqueous solutions of volatile weak electrolytes, AIChE Journal 24 (6) (1978) 966–976. doi:10.1002/aic.690240605.
URL https://doi.org/10.1002/aic.690240605

[64] U. Santo, D. Böning, M. Eberhard, H. Schmid, T. Kolb, Entrained flow gasification: experiments and balancing for design and scale-up, in: Proceedings of the 30th Deutscher Flammentag: für nachhaltige Verbrennung, 28-29 September 2021, Hannover-Garbsen, Germany, Deutsche Vereinigung für Verbrennungsforschung and The Combustion Institute Deutsche Sektion, Hannover-Garbsen, Germany, 2021. doi:10.5445/IR/1000139705.
URL https://doi.org/10.5445/IR/1000139705

[65] M. Dammann, M. Mancini, T. Kolb, R. Weber, Thermal radiation at high-temperature and high-pressure conditions: comparison of models for design and scale-up of entrained flow gasification processes, in: Proceedings of the 13th European Conference on Industrial Furnaces and Boilers, 19-22 April 2022, Algarve, Portugal, Algarve, Portugal, 2022. doi:10.5445/IR/1000145810.
URL https://doi.org/10.5445/IR/1000145810

[66] M. Dammann, M. Mancini, T. Kolb, R. Weber, Thermal radiation at high-temperature and high-pressure conditions: comparison of models for design and scale-up of entrained flow gasification processes, Thermal Sciences and Engineering Progress 40 (2023) 101772. doi:https://doi.org/10.1016/j.tsep.2023.101772.

[67] proFagus (2021). [link].
URL `https://profagus.de`

[68] K. Mielke, Über das Verhalten und die Kontrolle von Schlacken des bioliq-Vergasers, Ph.D. Thesis, Fakultät für Maschinenwesen, Rheinisch-Westfälische Technische Hochschule Aachen, Aachen, Germany (Apr. 2020).

[69] K. Mielke, G. Wu, M. Eberhard, T. Kolb, M. Müller, Optimization of slag mobility of biomass fuels in a pilot-scale entrained-flow gasifier, Chemical Engineering & Technology 44 (7) (2021) 1302–1310. `doi:10.1002/ceat.202000531`.
URL `https://doi.org/10.1002/ceat.202000531`

[70] M. Dammann, S. C. Walker, U. Santo, H. Knoch, M. Müller, M. Eberhard, M. Mancini, R. Weber, T. Kolb, Entrained flow gasification: slag property data for model validation (in preparation), Fuel.

[71] W. Wagner, International steam tables: properties of water and steam based on the industrial formulation IAPWS-IF97, 2nd Edition, Springer, Berlin, Germany [et al.], 2008. `doi:10.1007/978-3-540-74234-0`.
URL `https://doi.org/10.1007/978-3-540-74234-0`

[72] N. Y. Kirov, Specific heats and total heat contents of coals and related materials at elevated temperatures, BCURA Monthly Bulletin 29 (2) (1965) 33–59.

[73] Aspen Plus. Release V12 (2021).
URL `https://www.aspentech.com/products/aspen-plus.aspx`

[74] B. W. Brown, L. D. Smoot, P. J. Smith, P. O. Hedman, Measurement and prediction of entrained-flow gasification processes, AIChE Journal 34 (3) (1988) 435–446. `doi:10.1002/aic.690340311`.
URL `https://doi.org/10.1002/aic.690340311`

[75] W. Boie, Vom Brennstoff zum Rauchgas: feuerungstechnisches Rechnen mit Brennstoffkenngrössen und seine Vereinfachung mit Mitteln der Statistik, Teubner, Leipzig, Germany, 1957.

[76] M. Dammann, M. Mancini, R. Weber, T. Kolb, Entrained flow gasification: numerical simulations of pilot-scale experiments (in preparation), Fuel.

[77] S. Wachter, T. Jakobs, T. Kolb, Towards system pressure scaling of gas assisted coaxial burner nozzles – an empirical model, Applications in Energy and Combustion Science 5 (2021) 100019. `doi:10.1016/j.jaecs.2020.100019`.
URL https://doi.org/10.1016/j.jaecs.2020.100019

[78] F. Zhang, T. Zirwes, T. Müller, S. Wachter, T. Jakobs, P. Habisreuther, N. Zarzalis, D. Trimis, T. Kolb, Effect of elevated pressure on air-assisted primary atomization of coaxial liquid jets: basic research for entrained flow gasification, Renewable and Sustainable Energy Reviews 134 (2020) 110411. `doi:10.1016/j.rser.2020.110411`.
URL https://doi.org/10.1016/j.rser.2020.110411

Entrained flow gasification: pilot-scale experimental, balancing and equilibrium data for model validation

Maximilian Dammann[a,b,c,*], Ulrike Santo[b], David Böning[b], Hannah Knoch[b], Mark Eberhard[b], Thomas Kolb[a,b]

[a]*Karlsruhe Institute of Technology (KIT), Engler-Bunte-Institute, Fuel Technology (EBI ceb), Engler-Bunte-Ring 1, 76131 Karlsruhe, Germany*
[b]*Karlsruhe Institute of Technology (KIT), Institute for Technical Chemistry, Gasification Technology (ITC vgt), Hermann-von-Helmholtz-Platz 1, 76344 Eggenstein-Leopoldshafen, Germany*
[c]*Clausthal University of Technology, Institute for Energy Process Engineering and Fuel Technology (IEVB), Agricolastrasse 4, 38678 Clausthal-Zellerfeld, Germany*

Nomenclature

Latin symbols

a	activity
A	area
c	mass concentration
h	overall heat transfer coefficient
$\boldsymbol{h}$	overall heat transfer coefficient vector
H	inverse Henry constant
$\dot{H}$	enthalpy flow rate
I	ionic strength
K	constant
$\dot{m}$	mass flow rate
M	molar mass
$\dot{n}$	molar flow rate

*Corresponding author.
  ORCID: https://orcid.org/0000-0002-2851-7787.

p	pressure
P	input
$\dot{q}$	heat flux
$\dot{Q}$	heat flow rate
T	temperature
w	mass fraction
x	mole fraction
$\boldsymbol{x}$	mole fraction vector
x/L	relative nozzle distance
z	ion charge

Greek symbols

γ	activity coefficient
κ	electrical conductivity
ρ	density
φ	fugacity coefficient

Subscripts and superscripts

A	at position A
aq	aqueous
ash	of ash
asr	on an as-received basis
B	at position B
bal	balanced
Boie	based on Boie correlation
C	at position C
csp	in the purge stream for the cooling screen

diss	dissociation
dry	on a dry basis
eq	equilibrium
fuel	of fuel, in fuel
gas	gas, in the gas
i	of species i
in	at inlet
loss	lost
ng	of natural gas
ngb	at natural gas burner
op	operating
out	at outlet
quench	in the quench water
quench,prim	in the first quench spray ring
s	surface
sb	at slurry burner
Si	of segment i
slag	of slag, in slag
slurry	of slurry
steam	of steam
th	thermal
top	top
wall	wall
water	of liquid water
WGS	water-gas shift

ww,quench	of the waste water stream of the quench
ww,scrubber	of the waste water stream of the Venturi scrubber

Acronyms

bioliq EFG	bioliq Entrained Flow Gasifier
CC	carbon conversion
CGE	cold gas efficiency
COD	chemical oxygen demand
EFG	entrained flow gasifier
GC	gas chromatography
GRI	Gas Research Institute
HHV	higher heating value
LHV	lower heating value
SMOD	specific minimum oxygen demand
TIC	total inorganic carbon
TOC	total organic carbon
WGS	water-gas shift
Y	synthesis gas yield

S1. Supplementary data

S1.1. Methods

The thermal input of slurry $P_{\text{th,slurry}}$ and the thermal input of natural gas $P_{\text{th,ng}}$ are given by

$$P_{\text{th,slurry}} = \dot{m}_{\text{slurry}} \, \text{LHV}_{\text{slurry}} \,, \tag{S1}$$

$$P_{\text{th,ng}} = \dot{m}_{\text{ng}} \, \text{LHV}_{\text{ng}} \,, \tag{S2}$$

where $\dot{m}_{\text{slurry}}$ and $\dot{m}_{\text{ng}}$ are the mass flow rates of slurry and natural gas and $\text{LHV}_{\text{slurry}}$ and LHV_{ng} are the lower heating values of slurry and natural gas.

The stoichiometric ratio λ is defined by

$$\lambda = \frac{\dot{m}_{\text{O}_2}}{\dot{m}_{\text{slurry}} \, \text{SMOD}_{\text{slurry}} + \dot{m}_{\text{ng}} + \text{SMOD}_{\text{ng}}} \, , \tag{S3}$$

where $\dot{m}_{\text{O}_2}$ is the mass flow rate of oxygen and $\text{SMOD}_{\text{slurry}}$ and SMOD_{ng} are the specific minimum oxygen demands of slurry and natural gas.

Table S1: Composition of oxygen in mass fractions $\boldsymbol{w}_{\text{O}_2} = \left(w_{i,\text{O}_2}\right)$.

i	w_{i,O_2}
O_2	0.995
N_2	0.005

Table S2: Composition of nitrogen in mass fractions $\boldsymbol{w}_{\text{N}_2} = \left(w_{i,\text{N}_2}\right)$.

i	w_{i,N_2}
N_2	0.997
O_2	0.003

Table S3: Composition of natural gas in mass fractions $\boldsymbol{w}_{\mathrm{ng}} = w_{i,\mathrm{ng}}$.

i	$w_{i,\mathrm{ng}}$
CH_4	0.826509698
C_2H_6	0.098545845
C_3H_8	0.010531964
n-C_4H_{10}	0.001682183
i-C_4H_{10}	0.002478833
n-C_5H_{12}	0.000392293
i-C_5H_{12}	0.000600699
neo-C_5H_{12}	0.000020432
n-C_6H_{14}	0.000668673
CO_2	0.044867228
N_2	0.013702151

Table S4: Flow metres used for the streams.

Stream	Flow metre
Slurry	Coriolis flow metre (Endress+Hauser Promass 83)
Oxygen	Coriolis flow metre (Endress+Hauser Promass 83)
Nitrogen	Coriolis flow metre (Endress+Hauser Promass 83)
Natural gas	Coriolis flow metre (Endress+Hauser Promass 83)
Steam	Orifice metre (Endress+Hauser Deltatop DO62C)
Process water	Standard variable area flow metres (Krohne H250)
Waste water	Ultrasonic metres (Endress+Hauser Prosonic Flow)
Nitrogen for purging	Orifice metres (Endress+Hauser Deltatop DO62C) and standard variable area flow metres (Krohne H250)

Table S5: Standards used for the beech wood pyrolysis oil analyses II and VI.

Analysis	Standard
C, H, N	DIN 51732:2007 [1]
S	Based on DIN EN 15289:2011 [2]
Cl	Based on DIN 51727:2001 [3]
Water	DIN 51777-1:1983 [4]
Ash	Based on DIN 51719:1997 [5]
HHV	DIN 51900-2:2003 [6]

Table S6: Standards used for the beech wood pyrolysis oil analyses I, IV, VII and IX.

Analysis	Standard
C, H, N	DIN EN ISO 16948:2015 [7]
S	DIN EN ISO 10304-1:2009 [8]
Cl	DIN EN ISO 10304-1:2009 [8]
Water	Based on DIN 51777-1:1983 [4]
Ash	DIN 51719:1997 [5]
HHV	DIN 51900-2:2003 [6]

Table S7: Standards used for the beech wood pyrolysis oil analyses III, V, VIII and X.

Analysis	Standard
C, H, N	DIN EN 15104:2011 [9]
S	–
Cl	–
Water	ASTM E203-16 [10]
Ash	DIN 51719:1997 [5]
HHV	DIN EN 15400:2011 [11]

Table S8: Standards used for the waste water analyses.

Analysis	Standard
COD	DIN ISO 15705:2003 [12]
pH	DIN EN ISO 10523:2012 [13]
κ	DIN EN 27888:1993 [14]
Acetate	DIN EN ISO 10304-1:2009 [8]
Ammoniacal nitrogen	DIN 38406 5:1983 [15]
Boron	DIN EN ISO 11885:2009 [16]
Calcium	DIN EN ISO 11885:2009 [16]
Chloride	DIN EN ISO 10304-1:2009 [8]
Cyanide	DIN 38405-13:2011 [17]
Formate	DIN EN ISO 10304-1:2009 [8]
Magnesium	DIN EN ISO 11885:2009 [16]
Oxalate	DIN EN ISO 10304-1:2009 [8]
Phosphor	DIN EN ISO 11885:2009 [16]
Phosphate	DIN EN ISO 10304-1:2009 [8]
Potassium	DIN EN ISO 11885:2009 [16]
Silicon	DIN EN ISO 11885:2009 [16]
Sodium	DIN EN ISO 11885:2009 [16]
Sulphate	DIN EN ISO 10304-1:2009 [8]
Sulphur	DIN EN ISO 11885:2009 [16]
TIC	DIN EN 1484:1997 [18]
TOC	DIN EN 1484:1997 [18]
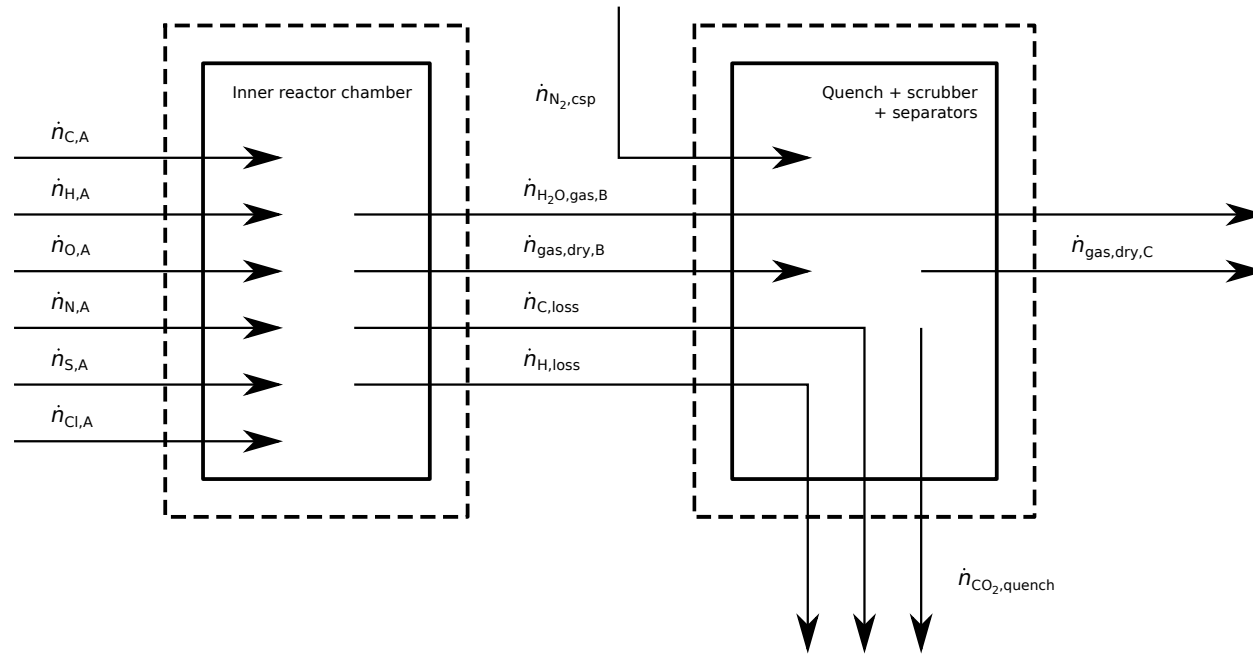
Figure S1: Elemental balancing of the bioliq EFG.
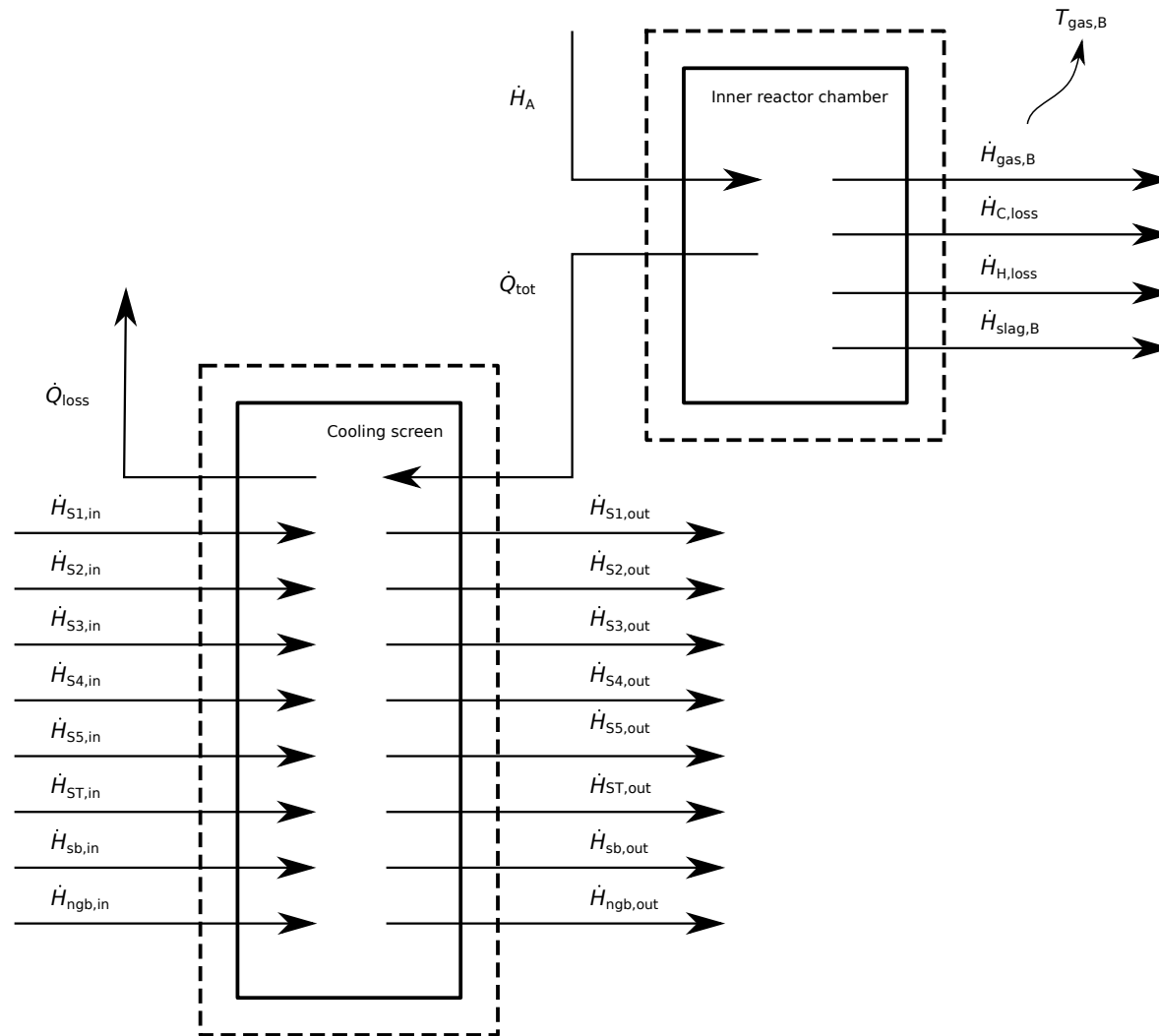
Figure S2: Energy balancing of the bioliq EFG.

Table S9: Compositions in mass fractions (as-received) based on various chemical analysis results for the beech wood pyrolysis oil.

Laboratory	$w_{\text{C,oil}}$	$w_{\text{H,oil}}$	$w_{\text{N,oil}}$	$w_{\text{S,oil}}$	$w_{\text{Cl,oil}}$	$w_{\text{ash,oil}}$	$w_{\text{H}_2\text{O,oil}}$
I	0.573	0.0614	–	–	–	0.001	0.056
II	0.581	0.0638	0.0014	0.00034	0.00009	0.001	0.054
III	0.576	0.0630	–	0.00010	0.00007	–	0.005
IV	0.571	0.0612	–	–	–	0.001	0.062
V	0.571	0.0648	–	0.00010	0.00007	–	0.004
VI	0.575	0.0637	0.0013	0.00022	0.00010	0.0001	0.060
VII	0.581	0.0625	–	–	–	0.001	0.043
VIII	0.584	0.0579	–	0.00008	0.00007	–	0.005
IX	0.573	0.0615	–	–	–	0.001	0.059
X	0.580	0.0670	–	0.00009	0.00007	–	0.005

Table S10: Higher heating values (as received) $\mathrm{HHV_{oil,asr}}$ based on various chemical analysis results for the beech wood pyrolysis oil, corresponding higher heating values based on the Boie correlation (as received) $\mathrm{HHV_{Boie,oil,asr}}$ and Boie ratios $\mathrm{HHV_{Boie,oil,asr}}/\mathrm{HHV_{oil,asr}}$.

Laboratory	$\dfrac{\mathrm{HHV_{oil,asr}}}{\mathrm{MJ/kg}}$	$\dfrac{\mathrm{HHV_{Boie,oil,asr}}}{\mathrm{MJ/kg}}$	$\dfrac{\mathrm{HHV_{Boie,oil,asr}}}{\mathrm{HHV_{oil,asr}}}$
I	24.262	23.750	0.979
II	24.500	24.407	0.996
III	24.276	23.528	0.969
IV	24.010	23.698	0.987
V	24.011	23.482	0.978
VI	24.322	24.172	0.994
VII	24.658	24.114	0.978
VIII	24.654	23.213	0.942
IX	24.104	23.795	0.987
X	24.065	24.188	1.005

Table S11: Feed data at position A: enthalpy flow rates of fuel $\dot{H}_{\mathrm{fuel,A}}$, enthalpy flow rates of natural gas $\dot{H}_{\mathrm{ng,A}}$, enthalpy flow rates of steam $\dot{H}_{\mathrm{steam,A}}$, enthalpy flow rates of O_2 $\dot{H}_{\mathrm{O_2,A}}$ and enthalpy flow rates of N_2 $\dot{H}_{\mathrm{N_2,A}}$ based on measurements. Reference conditions: 1 bar and 298.15 K.

Experiment	$\dfrac{\dot{H}_{\mathrm{fuel,A}}}{\mathrm{kW}}$	$\dfrac{\dot{H}_{\mathrm{ng,A}}}{\mathrm{kW}}$	$\dfrac{\dot{H}_{\mathrm{steam,A}}}{\mathrm{kW}}$	$\dfrac{\dot{H}_{\mathrm{O_2,A}}}{\mathrm{kW}}$	$\dfrac{\dot{H}_{\mathrm{N_2,A}}}{\mathrm{kW}}$
V82	3509.0	520.2	36.0	19.0	−1.8
V83	3488.3	520.4	35.2	17.8	−1.9
V84	3312.5	520.3	34.8	18.7	−2.0
V85	4425.1	520.2	34.6	19.6	−2.1

Table S12: Refractory temperatures at positions T1, T3, T5, T7 and T9 based on measurements.

Experiment	$\dfrac{T_{\text{wall,T1}}}{\text{K}}$	$\dfrac{T_{\text{wall,T3}}}{\text{K}}$	$\dfrac{T_{\text{wall,T5}}}{\text{K}}$	$\dfrac{T_{\text{wall,T7}}}{\text{K}}$	$\dfrac{T_{\text{wall,T9}}}{\text{K}}$
V82	862	896	936	972	954
V83	771	832	878	911	919
V84	867	906	954	961	958
V85	825	872	931	941	973

Table S13: Refractory temperatures at positions T2, T4, T6, T8 and T10 based on measurements.

Experiment	$\dfrac{T_{\text{wall,T2}}}{\text{K}}$	$\dfrac{T_{\text{wall,T4}}}{\text{K}}$	$\dfrac{T_{\text{wall,T4}}}{\text{K}}$	$\dfrac{T_{\text{wall,T8}}}{\text{K}}$	$\dfrac{T_{\text{wall,T10}}}{\text{K}}$
V82	903	894	978	972	924
V83	819	850	919	907	876
V84	901	898	968	954	901
V85	896	899	946	944	898

Table S14: Analysis results for the waste water samples of the quench: pH, electrical conductivity κ and concentrations of ammoniacal nitrogen, cyanide, acetate, formate, oxalate, TIC, TOC and sodium.

Experiment	pH	$\frac{\kappa}{\text{S/cm}}$	$\frac{c_{\text{ammoniacal nitrogen}}}{\text{mg/l}}$	$\frac{c_{\text{cyanide}}}{\text{mg/l}}$	$\frac{c_{\text{acetate}}}{\text{mg/l}}$	$\frac{c_{\text{formate}}}{\text{mg/l}}$	$\frac{c_{\text{oxalate}}}{\text{mg/l}}$	$\frac{c_{\text{TIC}}}{\text{mg/l}}$	$\frac{c_{\text{TOC}}}{\text{mg/l}}$	$\frac{c_{\text{sodium}}}{\text{mg/l}}$
V82	5.94	1060	45.3	0.25	< 10	384	< 10	109	104	123
V83	6.27	3630	32.5	0.07	< 10	1430	< 10	278	377	881
V84	6.23	2720	33.3	0.12	< 10	1130	< 10	122	310	567
V85	6.63	4680	217	2.47	< 10	2010	< 10	120	564	731

Table S15: Analysis results for the waste water samples of the Venturi scrubber: concentrations of TIC and TOC.

Experiment	$\frac{c_{\text{TIC}}}{\text{mg/l}}$	$\frac{c_{\text{TOC}}}{\text{mg/l}}$
V82	136	51
V83	106	43
V84	136	42
V85	113	99

Table S16: Heat flow rates $\dot{Q}_{\text{S1}}$, $\dot{Q}_{\text{S2}}$, $\dot{Q}_{\text{S3}}$, $\dot{Q}_{\text{S4}}$, $\dot{Q}_{\text{S5}}$ and $\dot{Q}_{\text{top}}$.

Experiment	$\frac{\dot{Q}_{\text{S1}}}{\text{kW}}$	$\frac{\dot{Q}_{\text{S2}}}{\text{kW}}$	$\frac{\dot{Q}_{\text{S3}}}{\text{kW}}$	$\frac{\dot{Q}_{\text{S4}}}{\text{kW}}$	$\frac{\dot{Q}_{\text{S5}}}{\text{kW}}$	$\frac{\dot{Q}_{\text{top}}}{\text{kW}}$
V82	76.15	154.90	212.27	37.52	35.21	28.46
V83	55.61	133.89	185.99	25.39	25.34	19.58
V84	68.29	154.84	208.88	34.68	33.76	23.68
V85	58.66	143.58	190.77	29.56	33.08	22.18

Table S17: Heat fluxes $\dot{q}_{\text{S1}}$, $\dot{q}_{\text{S2}}$, $\dot{q}_{\text{S3}}$, $\dot{q}_{\text{S4}}$ and $\dot{q}_{\text{S5}}$.

Experiment	$\frac{\dot{q}_{\text{S1}}}{\text{kW/m}^2}$	$\frac{\dot{q}_{\text{S2}}}{\text{kW/m}^2}$	$\frac{\dot{q}_{\text{S3}}}{\text{kW/m}^2}$	$\frac{\dot{q}_{\text{S4}}}{\text{kW/m}^2}$	$\frac{\dot{q}_{\text{S5}}}{\text{kW/m}^2}$
V82	71.92	103.67	125.22	77.48	115.11
V83	52.52	89.61	109.72	52.45	82.84
V84	64.50	103.64	123.23	71.62	110.34
V85	55.40	96.10	112.54	61.05	108.12

Table S18: Balanced cold gas efficiencies CGE_{bal}, equilibrium cold gas efficiencies CGE_{eq}, balanced yields Y_{bal} and equilibrium yields Y_{eq}.

Experiment	$\dfrac{CGE_{bal}}{\%}$	$\dfrac{CGE_{eq}}{\%}$	$\dfrac{Y_{bal}}{mol/kg}$	$\dfrac{Y_{eq}}{mol/kg}$
V82	55.1	55.8	37.2	37.8
V83	56.4	59.7	36.8	40.5
V84	48.7	53.6	31.4	34.8
V85	60.6	68.0	52.1	59.6

Table S19: Impact of the chemical analysis results of beech wood pyrolysis oil on the balancing results of the bioliq EFG experiments V85: water-gas shift temperatures at position B $T_{WGS,B}$, balanced temperatures at position B $T_{bal,B}$, equilibrium temperatures at position B $T_{eq,B}$, balanced cold gas efficiencies CGE_{bal} and balanced carbon conversions CC_{bal}.

Experiment	Laboratory	$\dfrac{T_{WGS,B}}{K}$	$\dfrac{T_{bal,B}}{K}$	$\dfrac{T_{eq,B}}{K}$	$\dfrac{CGE_{bal}}{\%}$	$\dfrac{CC_{bal}}{\%}$
V85	I	1550	1764	1696	60.9	96.1
	II	1607	1672	1578	60.6	93.4
	III	1477	1860	1803	60.5	97.7
	IV	1557	1721	1658	61.5	96.3
	V	1501	1813	1764	61.3	98.0
	VI	1610	1679	1598	61.0	94.4
	VII	1553	1776	1690	59.9	94.6
	VIII	1398	2014	1962	59.4	98.8
	IX	1560	1722	1653	61.3	95.9
	X	1556	1676	1595	61.2	94.8

S2. Geometry data

Table S20: Areas of the segments.

Segment	$\dfrac{A}{\mathrm{m^2}}$
S1	1.059
S2	1.494
S3	1.695
S4	0.484
S5	0.306
ST	0.318

Table S21: Relative nozzle distances of the thermocouples.

Thermocouple	$\dfrac{x}{L}$
T1	0.228
T2	0.243
T3	0.389
T4	0.364
T5	0.470
T6	0.485
T7	0.591
T8	0.606
T9	0.713
T10	0.728

S3. Freezing behaviour of WGS equilibrium in quench

S3.1. Methods

The freezing behaviour of the WGS equilibrium during the cooling of the synthesis gas was analysed for various bioliq EFG conditions using plug-flow

17

reactor simulations and WGS temperatures T_{WGS}. The simulations were carried out (i) using the GRI mechanism (version 3.0) [19], (ii) assuming various initial gas temperatures and two constant cooling rates, (iii) neglecting quenching effects except for cooling and (iv) assuming a typical synthesis gas equilibrium composition without hydrocarbons as initial gas composition. The lower cooling rate was estimated from gas temperature measurements at the outlet of an atmospheric entrained flow gasifier [20] while a much higher cooling rate can be expected for bioliq EFG conditions due to water quenching with a mass flow rate ratio of the water stream in the first spray ring to the synthesis gas stream above 1.6 (see Section S4). The WGS temperatures T_{WGS} for the kinetic calculations were derived using the thermodynamic data of the GRI mechanism (version 3.0) [19].

S3.2. Results

The pre-defined gas temperatures T_{gas} and the simulated WGS temperatures T_{WGS} are shown for two cooling rates and for five initial gas temperatures in Fig. S3. The freezing temperature accordingly increases with increasing cooling rate.
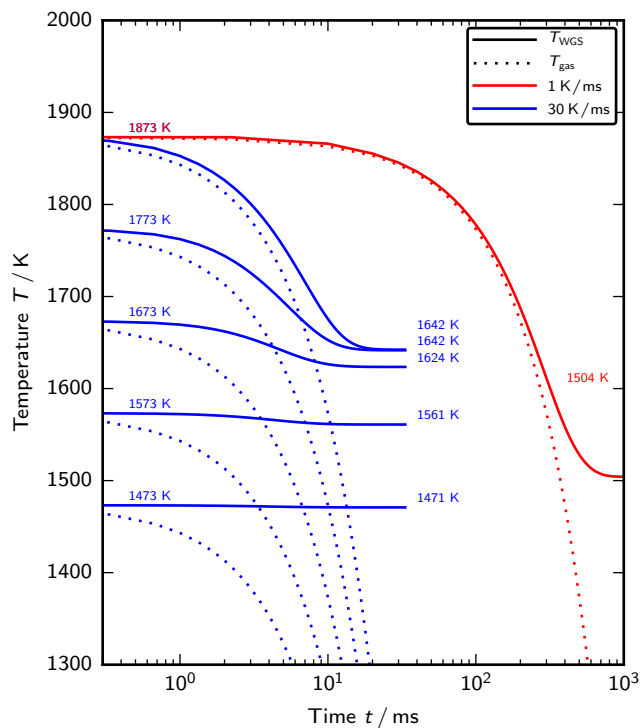
Figure S3: Pre-defined gas temperatures T_{gas} and predicted WGS temperatures T_{WGS} at cooling of synthesis gas assuming an initial synthesis gas composition, various initial gas temperatures and two cooling rates and based on plug-flow reactor simulations with the GRI mechanism (version 3.0) [19].

S4. Operating conditions of quench and Venturi scrubber

The operating conditions of the quench and the Venturi scrubber have an impact on the cooling rate of the synthesis gas, the waste water composition and thus the absorption capacity for dissolved synthesis gas components. Therefore, the operating parameters of the quench and the Venturi scrubber are summarised in Table S22 and are discussed below:

1. The circulating quench water was exchanged at regular intervals as

19

quench and Venturi scrubber installed were operated in discontinuous modes (which were the only possible operation modes). While waste water was discharged from the quench and the Venturi scrubber, fresh deionised water was supplied to minimise the impact of the quench water on the synthesis gas composition.

2. The mass flow rate ratio of quench water in the first spray ring to the synthesis gas after position B was always above 1.6 in each of the four bioliq EFG experiments. This typically ensures very fast cooling rates and suppresses water-gas shifts when passing the quench (see Section 2.2).

3. Different mass flow rates were applied for the discharges of waste water from the quench and the Venturi scrubber (and likewise for the supplies of fresh water) in the bioliq EFG experiments. Lower mass flow rates for the discharges of waste water typically lead to higher accumulation of dissolved synthesis gas components which can be detected by a higher electrical conductivity.

4. Supply of NaOH for neutralisation of the quench water was omitted during the periods of time with approximately stationary conditions of each of the four bioliq EFG experiments since basic components such as NaOH or NH_3 enhance the formation of formate in the quench water [21, 22], i.e. the supply of NaOH should be avoided to obtain most accurate balancing data. However, some NaOH was dosed to the quench water in the bioliq EFG experiments V83 and V85 a few hours before the stationary operating conditions. This could have caused higher formate concentrations than in the bioliq EFG experiments V82 and V84 and has affected the accuracy of the balancing data of the bioliq EFG experiments V83 and V85.

Table S22: Quench operating parameters: gas temperatures at quench outlet $T_{\text{gas,quench}}$, mass flow rate ratios of the water in the first spray ring to the synthesis gas at position B $\dot{m}_{\text{water,quench,prim}}/\dot{m}_{\text{gas,B}}$, mass flow rates of the waste water stream of the quench $\dot{m}_{\text{ww,quench}}$, mass flow rates of the waste water stream of the Venturi scrubber $\dot{m}_{\text{ww,scubber}}$, mass flow rates of NaOH into quench water $\dot{m}_{\text{NaOH,quench}}$ and pH based on measurements.

Experiment	$\dfrac{T_{\text{gas,quench}}}{\text{K}}$	$\dfrac{\dot{m}_{\text{water,quench,prim}}}{\dot{m}_{\text{gas,B}}}$	$\dfrac{\dot{m}_{\text{ww,quench}}}{\text{kg/h}}$	$\dfrac{\dot{m}_{\text{ww,scubber}}}{\text{kg/h}}$	$\dfrac{\dot{m}_{\text{NaOH,quench}}}{\text{kg/h}}$	pH
V82	479	1.62	1386	265	0	6.0
V83	477	1.66	1535	255	0	6.05
V84	478	1.60	1477	269	0	6.03
V85	477	1.62	922	408	0	6.2

S5. Solution equilibria of synthesis gas components in quench

S5.1. Methods

The mass concentration of species i in pure water c_i and the activity of species i in aqueous solutions a_i are described by

$$c_i = x_{i,\text{gas}}\,\varphi_{i,\text{gas}}\,\frac{p_{\text{gas}}}{H_i}\,\frac{M_i\,\rho_{\text{water}}}{M_{\text{water}}}\,, \tag{S4}$$

$$a_i = \gamma_i\,\frac{c_i}{M_i}\,, \tag{S5}$$

where $x_{i,\text{gas}}$ is the gas species mole fraction of species i, $\varphi_{i,\text{gas}}$ is the gas species fugacity coefficient of species i, p_{gas} is the gas pressure, H_i is the inverse Henry constant of species i, M_i is the molar mass of species i, ρ_{water} is the liquid density of water, M_{water} is the molar mass of water and γ_i is the activity coefficient of species i.

The inverse Henry constants of several synthesis gas species at ambient and pressurised conditions based on the property method ELECNRTL [23] are compared in Fig. S4. Accordingly, CO_2 shows a significantly higher solubility

than CH_4, CO, H_2 and N_2 and a lower solubility than NH_3 and HCN.
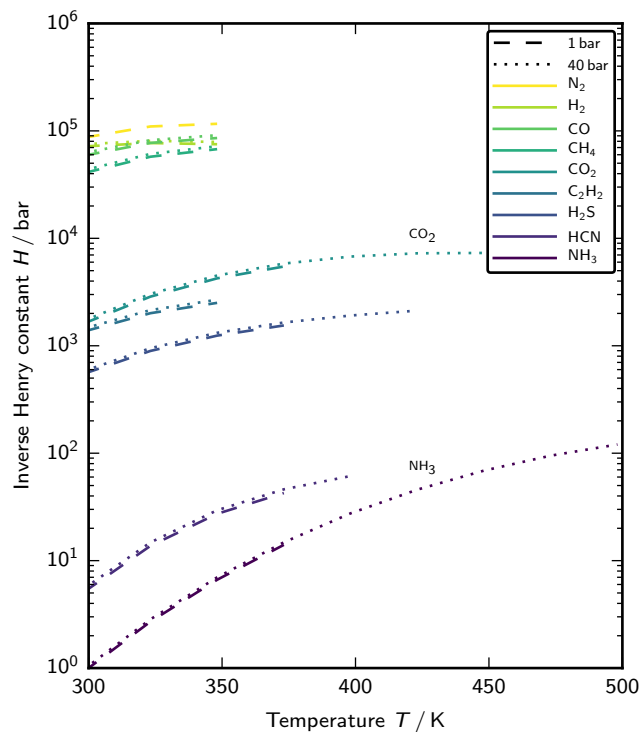
Figure S4: Predicted inverse Henry constants H of synthesis gas components based on the property method ELECNRTL.

The acid-base equilibrium between CO_2 and NH_3 enhances the dissociation of dissolved CO_2 into the various forms of carbonic acid and of dissolved NH_3 into basic ammonium. As very low amounts of ammonia are expected to be present in the synthesis gas from surrogate fuels, only the solution equilibria of CO_2

$$CO_2(aq) + H_2O(l) \rightleftharpoons H^+(aq) + HCO_3^-(aq), \tag{S6}$$

$$HCO_3^-(aq) \rightleftharpoons H^+(aq) + CO_3^{2-}(aq), \tag{S7}$$
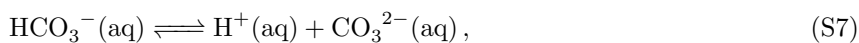
are accounted for in this study and are described by temperature- and pressure-

dependent dissociation constants

$$K_{\text{diss},1}(T,p) = \frac{a_{\text{H}^+(\text{aq})}\, a_{\text{HCO}_3^-(\text{aq})}}{a_{\text{CO}_2(\text{aq})}} \,, \tag{S8}$$

$$K_{\text{diss},2}(T,p) = \frac{a_{\text{H}^+(\text{aq})}\, a_{\text{CO}_3^{2-}(\text{aq})}}{a_{\text{HCO}_3^-(\text{aq})}} \tag{S9}$$

at process conditions [24, 25], where $a_{\text{H}^+(\text{aq})}$, $a_{\text{HCO}_3^-(\text{aq})}$, $a_{\text{CO}_2(\text{aq})}$ and $a_{\text{CO}_3^{2-}(\text{aq})}$ are the activities of dissolved H^+, HCO_3^-, CO_2 and CO_3^{2-} in aqueous solutions, respectively. The activity of dissolved CO_2, which can be determined from the concentrations of the diluted salts [26], is one for very low concentrated solutions, whereas the activities of dissolved H^+, HCO_3^- and CO_3^{2-} are described using activity coefficients. The activity coefficient of species i γ_i is calculated by [27, 28]

$$\lg(\gamma_i) = -A\, z_i^2\, \frac{\sqrt{I}}{1+\sqrt{I}} - 0.3\, I \quad \text{for} \quad I < 0.5\, \frac{\text{mol}}{\text{l}}\,, \tag{S10}$$

where

$$A = 1.82 \cdot 10^6 \left(88.50\, \exp\left(-0.004665\, \frac{T - 273.15\,\text{K}}{\text{K}} \right) \frac{T}{\text{K}} \right)^{-3/2}, \tag{S11}$$

is a temperature-dependent parameter for process conditions and I is the ionic strength and z_i is the ion charge of the species i. For aqueous solutions, the ionic strength I is defined by [29]

$$I = \frac{1}{2} \sum_i \frac{c_i}{M_i}\, z_i^2\,, \tag{S12}$$

where the summation is performed over all ions prevailing in the solution. However, if not all ions and their concentrations are known, the ion strength I can be estimated from the electrical conductivity κ which increases with increasing ion concentrations. For low concentrated solutions, the ionic strength I is given by [29]

$$\lg\left(\frac{I}{\text{mol/l}} \right) = -1.841 + 1.009\, \lg\left(\frac{\kappa}{\text{mS/cm}} \right) \quad \text{for} \quad I < 0.2\, \frac{\text{mol}}{\text{l}}. \tag{S13}$$

The mass concentration of TIC c_{TIC} is the sum of mass concentrations of carbon in dissolved molecular and dissociated carbon dioxide and is defined by

$$c_{\text{TIC}} = M_{\text{C}} \left(\frac{c_{\text{CO}_2(\text{aq})}}{M_{\text{CO}_2}} + \frac{c_{\text{HCO}_3^-(\text{aq})}}{M_{\text{HCO}_3^-}} + \frac{c_{\text{CO}_3^{2-}(\text{aq})}}{M_{\text{CO}_3^{2-}}} \right), \tag{S14}$$

23

where $c_{CO_2(aq)}$, $c_{HCO_3^-(aq)}$ and $c_{CO_3^{2-}(aq)}$ are the mass concentrations of dissolved CO_2, HCO_3^- and CO_3^{2-}, respectively. Then, inserting Eqs. (S4), (S8) and (S9) into Eq. (S14) and assuming $\gamma_{H^+(aq)} = \gamma_{HCO_3^-(aq)}$ due to the same charge, the equilibrium mass concentration of TIC $c_{TIC,eq}$ is given by

$$
\begin{aligned}
c_{TIC,eq} = M_C \left(x_{CO_2,gas}\, \varphi_{CO_2,gas}\, \frac{p_{gas}}{H_{CO_2}}\, \frac{\rho_{water}}{M_{water}} \right) \left(\frac{1}{\gamma_{CO_2(aq)}} \right. \\
\left. + \frac{K_{diss,1}\, M_{CO_2}\, M_{H^+(aq)}}{c_{H^+(aq)}\, \gamma_{H^+(aq)}^2} + \frac{K_{diss,1}\, K_{diss,2}\, M_{H^+(aq)}^2}{c_{H^+(aq)}^2\, \gamma_{CO_3^{2-}(aq)}^2\, \gamma_{H^+(aq)}^2} \right).
\end{aligned}
\tag{S15}
$$

The equilibrium mass concentration of TIC $c_{TIC,eq}$ thus depends on the measured dry gas species concentration of CO_2 $x_{CO_2,gas}$, the inverse Henri constant of CO_2 H_{CO_2}, the dissociation constants, the pH and the ionic strength.

Since pH and ionic strength could not be determined at process conditions in this study, the equilibrium mass concentration of TIC $c_{TIC,eq}$ was estimated using (i) pH and electrical conductivity κ of the waste water samples, collected and analysed at ambient conditions (see Section 3.1.2), (ii) literature data for the inverse Henry constant of CO_2 [30] and the dissociation constants [24] and (iii) iterative calculations. Firstly, the ionic strength I was determined from the electrical conductivity κ of the waste water samples using Eq. (S13). Subsequently, the ionic strength I was corrected for the change of the mass concentration of TIC $\Delta c_{TIC} = c_{TIC,eq} - c_{TIC,meas}$ by

$$
I := I + \frac{1}{2} \left(\frac{\Delta c_{HCO_3^-(aq)}}{M_{HCO_3^-(aq)}} + 4\, \frac{\Delta c_{CO_3^{2-}(aq)}}{M_{CO_3^{2-}(aq)}} \right). \tag{S16}
$$

Corrections were only applied for the ionic strength I, while corrections were not performed for pH because of the buffering or balancing effects of alkaline components such as $NaOH$ and NH_3 in the quench water.

For verification of calculated equilibrium mass concentrations of TIC $c_{TIC,eq}$, mass concentrations of TIC were derived from measurements under ambient conditions and from elemental balancing at process conditions. The measured mass concentrations of TIC $c_{TIC,meas}$ were obtained based on DIN EN 1484:1997 [18] (see Section 3.1.2), while the balanced total inorganic

24

carbon content $c_{\text{TIC,bal}}$ was determined by

$$c_{\text{TIC,bal}} = \frac{\dot{m}_{\text{CO}_2,\text{quench}}\, M_{\text{C}}}{(\dot{V}_{\text{ww,quench}} + \dot{V}_{\text{ww,scrubber}})M_{\text{CO}_2}}\,, \tag{S17}$$

where $\dot{m}_{\text{CO}_2,\text{quench}}$ is the balanced mass flow rate of dissolved and dissociated CO_2 (see Sections 3.4) and $\dot{V}_{\text{ww,quench}}$ and $\dot{V}_{\text{ww,scrubber}}$ are the measured volume flow rates of the waste water streams of the quench and the Venturi scrubber, respectively.

S5.2. Results

The influence of the process, sampling and analysis conditions on the solution and dissociation of CO_2 in the quench water was investigated considering the bioliq EFG experiment V82 with low contents of dissolved salts. Firstly, solution and dissociation equilibria in the presence of highly diluted quench water were calculated for various conditions faced by quench water during operation, sampling and analysis: (i) the initial process condition at $483\,\text{K}$ and $40\,\text{bar}$, (ii) the condition after cooling under pressure to $407\,\text{K}$ in the circulation, (iii) the sampling condition after depressurisation and (iv) the analysis condition. The calculated equilibrium TIC concentrations $c_{\text{TIC,eq}}$ at the four conditions are shown as function of pH in Fig. S5 and are compared with measured and balanced TIC concentrations of the quench water. Accordingly, the measured TIC concentrations $c_{\text{TIC,meas}}$ of all waste water samples are close to the equilibrium TIC concentrations $c_{\text{TIC,eq}}$ at ambient conditions. Thus, if a higher TIC concentration has prevailed at process conditions, this concentration cannot be detected by TIC analysis of waste water samples. Higher TIC contents likely degas and do not remain in the samples until analysis. Therefore, the TIC analysis of waste water samples after expansion and cooling does not provide any information about the TIC concentration under process conditions. Furthermore, the balanced TIC concentration $c_{\text{TIC,bal}}$ for the bioliq EFG experiment V82 is in good agreement with the equilibrium TIC concentration $c_{\text{TIC,eq}}$ at quench conditions. Thus, the iterative calculation of the solution and dissociation of CO_2 is

appropriate in the presence of quench waters with very low salt concentrations and electrical conductivities, while future studies should focus on the solution and dissociation in the presence of higher concentrated quench waters to verify the balanced TIC concentrations $c_{\mathrm{TIC,bal}}$ between $4\,\mathrm{g/l}$ and $8\,\mathrm{g/l}$ in the bioliq EFG experiments V83, V84 and V85.
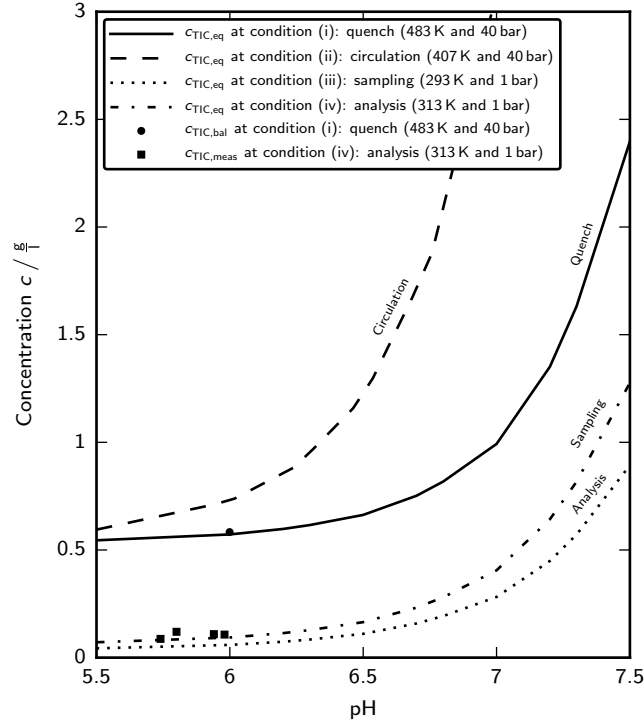
Figure S5: Equilibrium TIC concentrations $c_{\mathrm{TIC,eq}}$, balanced TIC concentration $c_{\mathrm{TIC,bal}}$ and measured TIC concentrations $c_{\mathrm{TIC,meas}}$: comparison for the bioliq EFG experiment V82.

S6. Time histories of measurement data

The time histories of the measurement data were used to investigate the system behaviour during start-up and to determine the periods of time with approximately stationary conditions. Specifically, the time histories of the

refractory temperatures and the dry gas species concentrations at position C are appropriate to access the stationarity of the inner reactor chamber and are shown for the bioliq EFG experiment V85 in Figs. S6 and S7. Note that (i) grey boxes mark the periods of time considered in the balancing and equilibrium calculations and the intervals for calibration and maintenance of the gas chromatograph and (ii) broken lines indicate the start times for constant operating settings and the times of waste water sampling.

The time histories in Fig. S6 show that the refractory temperatures were slightly increasing for more than two days. This indicates changes of both the gas temperature distribution in the inner reactor chamber and the slag deposition. Furthermore, this can be attributed to changes of the beech wood pyrolysis oil composition and to corresponding slight adjustments of the operating conditions.

The time histories in Fig. S7 show that the dry gas species concentrations of CO, CO_2, H_2 and N_2 quickly reach stationary levels and slightly reflect changes of the operating conditions, while the dry gas species concentration of CH_4 decreases corresponding to the likely increase of the gas temperature in the inner reactor chamber.
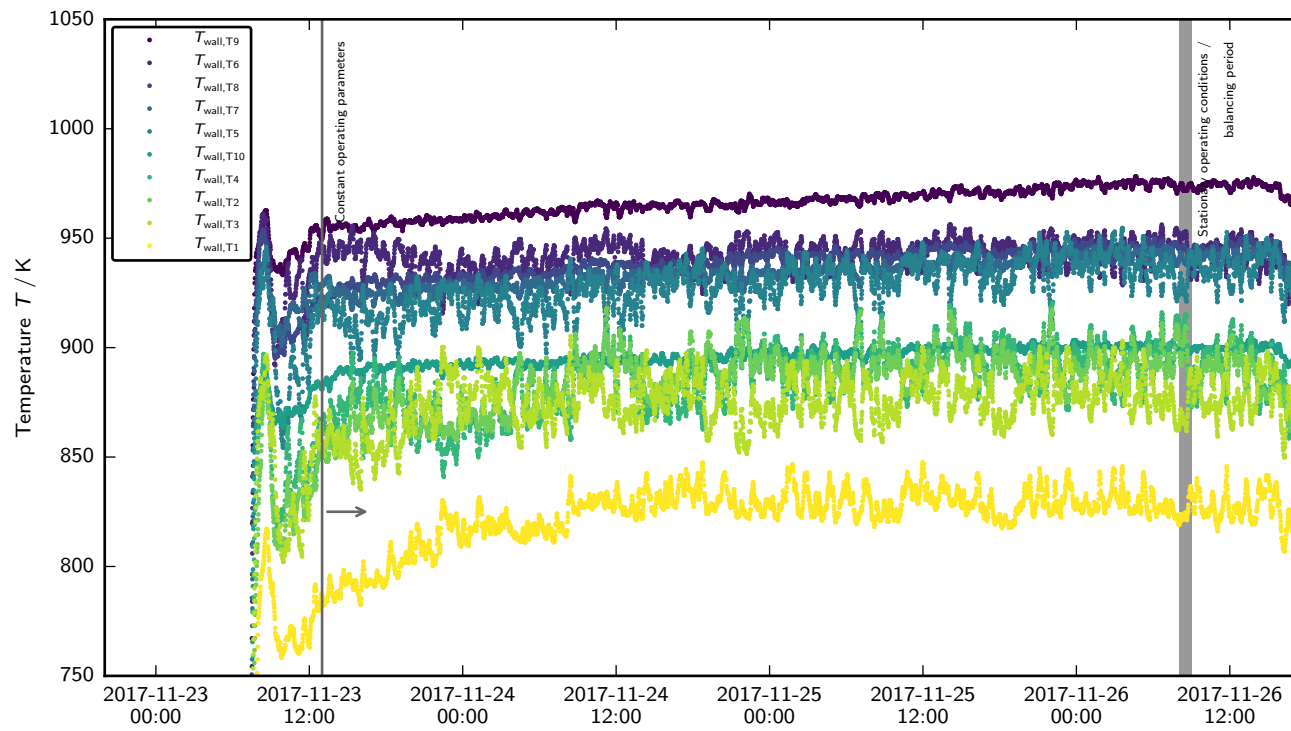
Figure S6: Time histories of the refractory temperatures: comparison for the bioliq EFG experiment V85.
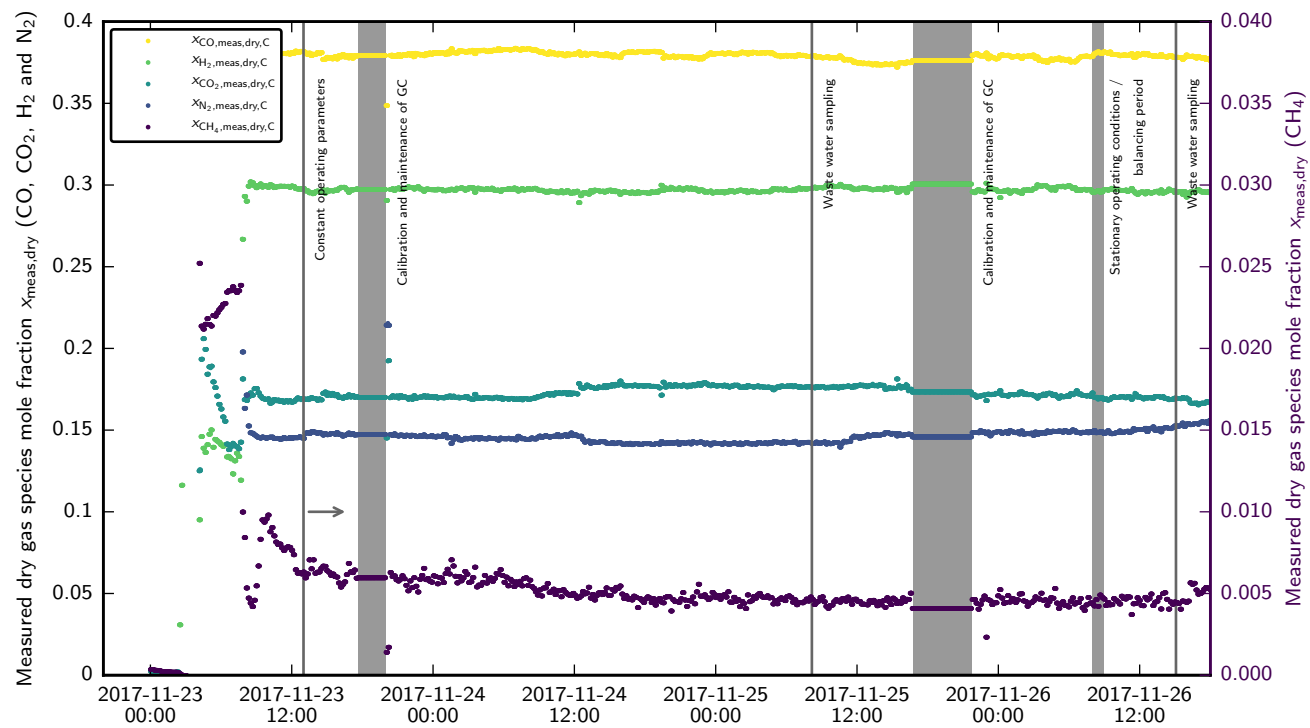
Figure S7: Time histories of the measured dry gas species concentrations in mole fractions: comparison for the bioliq EFG experiment V85.

References

[1] DIN Deutsches Institut für Normung, DIN 51732:2007-08. Prüfung fester Brennstoffe. Bestimmung des Gesamtgehaltes an Kohlenstoff, Wasserstoff und Stickstoff. Instrumentelle Methoden (Aug. 2007).

[2] DIN Deutsches Institut für Normung, DIN EN 15289:2011-04. Feste Biobrennstoffe. Bestimmung des Gesamtgehaltes an Schwefel und Chlor (Apr. 2011).

[3] DIN Deutsches Institut für Normung, DIN 51727:2001-06. Prüfung fester Brennstoffe. Bestimmung des Chlorgehaltes (Jun. 2001).

[4] DIN Deutsches Institut für Normung, DIN 51777-1:1983-03. Prüfung von Mineralöl-Kohlenwasserstoffen und Lösennitteln. Bestimmung des Wassergehaltes durch Titration nach Karl Fischer. Direktes Verfahren (Mar. 1983).

[5] DIN Deutsches Institut für Normung, DIN 51719:1997-07. Prüfung fester Brennstoffe. Bestimmung des Aschegehaltes (Jul. 1997).

[6] DIN Deutsches Institut für Normung, DIN 51900-2:2003-03. Prüfung fester und flüssiger Brennstoffe. Bestimmung des Brennwertes mit dem Bomben-Kalorimeter und Berechnung des Heizwertes. Teil 2: Verfahren mit isoperibolem oder static-jacket Kalorimeter (Mar. 2003).

[7] DIN Deutsches Institut für Normung, DIN EN ISO 16948:2015-09. Biogene Festbrennstoffe. Bestimmung des Gesamtgehaltes an Kohlenstoff, Wasserstoff und Stickstoff (ISO 16948:2015) (Sep. 2015).

[8] DIN Deutsches Institut für Normung, DIN EN ISO 10304-1:2009-07. Wasserbeschaffenheit. Bestimmung von gelösten Anionen mittels Flüssigkeits-Ionenchromatographie. Teil 1: Bestimmung von Bromid, Chlorid, Fluorid, Nitrat, Nitrit, Phosphat und Sulfat (ISO 10304-1:2007) (Jul. 2009).

[9] DIN Deutsches Institut für Normung, DIN EN 15104:2011-04. Feste Biobrennstoffe. Bestimmung des Gesamtgehaltes an Kohlenstoff, Wasserstoff und Stickstoff. Instrumentelle Verfahren (Apr. 2011).

[10] ASTM International, ASTM E203-16. Standard test method for water using volumetric Karl Fischer titration (2016). `doi:10.1520/E0203-16`. URL `https://doi.org/10.1520/E0203-16`

[11] DIN Deutsches Institut für Normung, DIN EN 15400:2011-05. Feste Sekundärbrennstoffe. Bestimmung des Brennwertes (Nov. 2011).

[12] DIN Deutsches Institut für Normung, DIN ISO 15705:2003-01. Bestimmung des chemischen Sauerstoffbedarfs (ST-CSB) (ISO 15705:2002) (Jan. 2003).

[13] DIN Deutsches Institut für Normung, DIN EN ISO 10523:2012-04. Wasserbeschaffenheit. Bestimmung des pH-Werts (ISO 10523:2008) (Apr. 2012).

[14] DIN Deutsches Institut für Normung, DIN EN 27888:1993-11. Wasserbeschaffenheit. Bestimmung der elektrischen Leitfähigkeit (ISO 7888:1985) (Nov. 1993).

[15] DIN Deutsches Institut für Normung, DIN 38406-5:1983-10. Kationen (Gruppe E). Bestimmung des Ammonium-Stickstoffs (E5) (Oct. 1983).

[16] DIN Deutsches Institut für Normung, DIN EN ISO 11885:2009-09. Wasserbeschaffenheit. Bestimmung von ausgewählten Elementen durch induktiv gekoppelte Plasma-Atom-Emissionsspektrometrie (ICP-OES) (ISO 11885:2007) (Sep. 2009).

[17] DIN Deutsches Institut für Normung, DIN 38405-13:2011-04. Deutsche Einheitsverfahren zur Wasser-, Abwasser- und Schlammuntersuchung. Anionen (Gruppe D). Teil 13: Bestimmung von Cyaniden (D 13) (Apr. 2011).

[18] DIN Deutsches Institut für Normung, DIN EN 1484:1997-08. Wasseranalytik. Anleitungen zur Bestimmung des gesamten organischen Kohlenstoffs (TOC) und des gelösten organischen Kohlenstoffs (DOC) (Aug. 1997).

[19] G. P. Smith, D. M. Golden, M. Frenklach, N. W. Moriarty, B. Eiteneer, M. Goldenberg, C. T. Bowman, R. K. Hanson, S. Song, W. Gardiner, V. V. Lissianski, Z. Qin, GRI-Mech 3.0 (1999).
URL http://combustion.berkeley.edu/gri-mech/

[20] S. Fleck, U. Santo, C. Hotz, T. Jakobs, G. Eckel, M. Mancini, R. Weber, T. Kolb, Entrained flow gasification. Part 1: gasification of glycol in an atmospheric-pressure experimental rig, Fuel 217 (2018) 306–319. doi:10.1016/j.fuel.2017.12.077.
URL https://doi.org/10.1016/j.fuel.2017.12.077

[21] P. Brüggemann, Formation and evolution of by-products and trace substances in the high pressure partial oxidation of gaseous and liquid hydrocarbons, Ph.D. Thesis, Fakultät für Maschinenbau, Technische Universität Bergakademie Freiberg, Freiberg, Germany (Sep. 2010).

[22] C. Ehnes, Heterogen katalysierte Hydrierung von Kohlendioxid zu Ameisensäure, Ph.D. Thesis, Fachbereich Chemie, Technische Universität Darmstadt, Darmstadt, Germany (Jul. 2016).
URL https://tuprints.ulb.tu-darmstadt.de/5634

[23] Aspen Properties. Release V12 (2022).
URL https://www.aspentech.com/products/aspen-properties.aspx

[24] T. J. Edwards, G. Maurer, J. Newman, J. M. Prausnitz, Vapor-liquid equilibria in multicomponent aqueous solutions of volatile weak electrolytes, AIChE Journal 24 (6) (1978) 966–976. doi:10.1002/aic.690240605.
URL https://doi.org/10.1002/aic.690240605

[25] A. J. Read, The first ionization constant of carbonic acid from 25 to 250 °C and to 2000 bar, Journal of Solution Chemistry 4 (1) (1975) 53–70. `doi: 10.1007/bf00646052`.
URL `https://doi.org/10.1007/BF00646052`

[26] S. Weisenberger, A. Schumpe, Estimation of gas solubilities in salt solutions at temperatures from 273 K to 363 K, AIChE Journal 42 (1) (1996) 298–300.

[27] W. Stumm, J. J. Morgan, Aquatic chemistry: chemical equilibria and rates in natural waters, 3rd Edition, Wiley, New York, NY, USA [et al.], 1996.

[28] F. Booth, The dielectric constant of water and the saturation effect, The Journal of Chemical Physics 19 (4) (1951) 391–394. `doi:10.1063/1. 1748233`.
URL `https://doi.org/10.1063/1.1748233`

[29] G. Sposito, The chemistry of soils, 2nd Edition, Oxford University Press, New York, NY, USA [et al.], 2008.

[30] R. Crovetto, Evaluation of solubility data of the system CO_2-H_2O from 273 K to the critical point of water, Journal of Physical and Chemical Reference Data 20 (3) (1991) 575–589. `doi:10.1063/1.555905`.